



## Research Article

# Microstructural, structural, dielectric, piezoelectric and energy storage properties of 0.2 wt% MnO<sub>2</sub> doped (0.94-x)Na<sub>0.5</sub>Bi<sub>0.5</sub>TiO<sub>3</sub>-0.06BaTiO<sub>3</sub>-xK<sub>0.5</sub>Na<sub>0.5</sub>NbO<sub>3</sub> ceramics (0 ≤ x ≤ 0.08)

Getaw Abebe<sup>1,2</sup> · Gudeta Jafo<sup>1,2</sup> · Gobinda Das Adhikary<sup>1</sup> · Arnab De<sup>1</sup> · Rajeev Ranjan<sup>1</sup> · Anupam Mishra<sup>1</sup> 

Received: 9 July 2020 / Accepted: 20 October 2020 / Published online: 2 November 2020  
© Springer Nature Switzerland AG 2020

## Abstract

Lead free (0.94-x)Na<sub>0.5</sub>Bi<sub>0.5</sub>TiO<sub>3</sub>-0.06BaTiO<sub>3</sub>-xK<sub>0.5</sub>Na<sub>0.5</sub>NbO<sub>3</sub> ceramics are under the spotlight owing to their multifunctional nature. We have systematically investigated the microstructural, structural, dielectric, piezoelectric and energy storage properties of the system in the range 0 ≤ x ≤ 0.08. There is a systematic reduction in grain size with increasing K<sub>0.5</sub>Na<sub>0.5</sub>NbO<sub>3</sub>(KNN) concentration. The enhancement in disorder with K<sub>0.5</sub>Na<sub>0.5</sub>NbO<sub>3</sub>(KNN) doping is evident from the increase in slope of the dielectric dispersion plots. The unpoled compositions have a cubic like structure in the whole range i.e. from x = 0 to x = 0.08. However, the application of electric field (poling) results in a structural transformation to lower symmetry upto x = 0.04. Beyond that the disorder dominates over the applied electric field and the structure is cubic like even in the poled state. The energy storage density increases from 0.08 J/cm<sup>3</sup> for x = 0 to 1.19 J/cm<sup>3</sup> for x = 0.05 and saturates thereafter. Discharge efficiency also follows a similar trend. The piezoresponse decreases with KNN doping from 151 pC/N for x = 0 to 4 pC/N for x = 0.08. It is observed that energy storage density and piezoresponse are complementary properties which increase at the expense of each other.

**Keywords** Grain size · Ceramics · Energy storage density · Discharge efficiency · Piezoresponse

## 1 Introduction

The need of energy is rapidly increasing in a world with expanding industrialization, increasing globalization and a fast-growing population [1, 2]. The continuous growth in demand for miniaturization and compactness in electronic devices have resulted in more focused research on finding high energy storage materials [3]. Relaxor/antiferroelectric materials are finding use in pulsed power capacitors (PPC) and multilayer ceramic capacitors (MLCC) owing to their low remnant polarization and coercive field [4–6]. Pb(Zr,Sn,Ti)O<sub>3</sub> (PZST), (Pb,La)(Zr,Ti)O<sub>3</sub> (PLZT) and (Pb,La)ZrO<sub>3</sub> (PLZ) based relaxor/antiferroelectric systems have shown very high energy storage properties and have been extensively investigated [7–9]. However, lead is toxic and

carcinogenic in nature and off-late stringent governmental legislations have been enforced thereby restricting its use [10, 11]. Therefore, researchers have been putting extensive efforts to find suitable lead-free alternatives [12–14]. BaTiO<sub>3</sub>, AgNbO<sub>3</sub> and Na<sub>0.5</sub>Bi<sub>0.5</sub>TiO<sub>3</sub> (NBT) based lead-free systems are under the radar as potential candidates for application in energy storage devices [15–20]. However BaTiO<sub>3</sub> based systems have a lower working range and AgNbO<sub>3</sub> based systems are expensive to synthesize [21, 22]. This makes NBT based materials one of the viable alternatives to lead based ones [23–25]. Discovered in 1961 by Smolenski et al., research on NBT has surged in the past two decades [13, 14, 26, 27]. NBT has a high saturation polarization (P<sub>s</sub>) of 40 μC/cm<sup>2</sup>, high coercive field (E<sub>c</sub>) of 55 kV/cm, a moderate piezoelectric response (d<sub>33</sub>) of 75

✉ Anupam Mishra, mishraanupam0@gmail.com | <sup>1</sup>Department of Materials Engineering, Indian Institute of Science, Bangalore 560012, India. <sup>2</sup>Faculty of Materials Science and Engineering, Jimma Institute of Technology, Jimma, Ethiopia.



pC/N and a depolarization temperature ( $T_d$ ) of 190 °C [28]. However, the issue of leakage current and a high coercive field (55 kV/cm) limits the industrial and technological applications of NBT [29, 30]. Researchers have sought to overcome this problem by doping NBT with suitable dopants like BaTiO<sub>3</sub>(BT), K<sub>0.5</sub>Na<sub>0.5</sub>NbO<sub>3</sub>(KNN), SrTiO<sub>3</sub>(ST) in order to reduce its coercive field and improve its functionality [14, 31–33]. In the BT doped NBT family the composition NBT-6BT(0.94(Na<sub>0.5</sub>Bi<sub>0.5</sub>TiO<sub>3</sub>)-0.06BaTiO<sub>3</sub>) has been under intense scrutiny as it is a morphotropic phase boundary (MPB) composition showing high piezoresponse ( $d_{33} = 200$  pC/N) [34–37]. KNN has been doped into NBT-6BT matrix with an intent to further enhance and modulate its properties according to need [38–41]. Some of the researchers have shown the potential of KNN doped NBT-6BT alloy in room temperature and high temperature energy storage applications [42–47]. The energy storage behavior of 1, 2 and 5 mol% KNN doped NBT-6BT compositions have been particularly emphasized in these reports [41–45]. However, a systematic study showing the gradual effect of KNN doping on the energy storage properties of NBT-6BT is still missing. There is no report available to the best of our knowledge which correlates structural, dielectric, piezoelectric and energy storage properties of NBT-6BT-KNN system. In this paper we have carried out a systematic study on the effect of KNN doping on the structure, microstructure, dielectric, piezoelectric and energy storage properties of NBT-6BT. An effort has also been made to find the inherent correlation between these properties. As a part of our strategy, KNN was doped with an intention to induce disorder in the NBT-6BT matrix and drive the system towards a relaxor ferroelectric state. The compositions were synthesized according to the nominal formulae (0.94-x)NBT-0.06BT-xKNN. The samples are named according to the mol% of KNN doped in the NBT-6BT matrix. For example, 0.94NBT-0.06BT is termed as 0KNN and 0.89NBT-0.06BT-0.05KNN is named as 5KNN. 0.2 wt% MnO<sub>2</sub> was added to the calcined powder with an intention to improve the densification of the ceramics and to reduce leakage current. It was found that the energy storage density and the discharge efficiency improves till 5KNN beyond that the properties get stabilized/saturated. The structural/chemical disorder which is mathematically quantified from the magnitude of slope of the dielectric dispersion plot, increases drastically till 5KNN and gradually saturates thereafter. It was also observed that piezoresponse drastically deteriorated beyond 5KNN. The energy storage properties of the compositions 0KNN and 5KNN were also studied as a function of temperature and the upper working limit was found to be 100 °C. We found that the piezoresponse and energy storage density are complementary properties which improve at the expense of each other. While presence of structural disorder is beneficial

for the energy storage properties, it proves detrimental for the piezoresponse.

## 2 Experimental procedure

The polycrystalline specimens of the (0.94-x)NBT-0.06BT-xKNN ( $0 \leq x \leq 0.08$ ) series were prepared by the conventional solid-state ceramic synthesis route. Dried powders of Na<sub>2</sub>CO<sub>3</sub> (99.8%, Alfa Aesar), Bi<sub>2</sub>O<sub>3</sub> (99%, SRL), TiO<sub>2</sub> (99.8%, Alfa Aesar), BaCO<sub>3</sub> (99.8%, Alfa Aesar), K<sub>2</sub>CO<sub>3</sub> (99%, Alfa Aesar) and Nb<sub>2</sub>O<sub>5</sub> (99.9%, Alfa Aesar) were weighed according to their stoichiometry and ball milled in planetary ball mill (Fritsch, P5) for 12 h in acetone medium for homogenization using yttria stabilized zirconia (YSZ) vials aided with yttria stabilized zirconia (YSZ) balls at a speed of 200 rpm. The ball milled powders were then dried and calcined in muffle furnace for 900 °C for 3 h in covered alumina crucibles. The calcined powder was again re-ball milled for 8 h followed by recalcination at 900 °C for 3 h to ensure complete perovskite phase formation. The comparative XRPD plots of 1st step and 2nd step calcined powder of 5KNN are shown in Fig. 1. A peak corresponding to a secondary non perovskite phase is observed at 28° after 1st step calcination. The peak completely disappears after 2nd stage calcination and only perovskite peaks are observed. 0.2 wt% MnO<sub>2</sub> (99.9%, Alfa Aesar) was added to the recalcined powders following which 2% (w/v) Poly-Vinyl Alcohol (PVA) binder was mixed

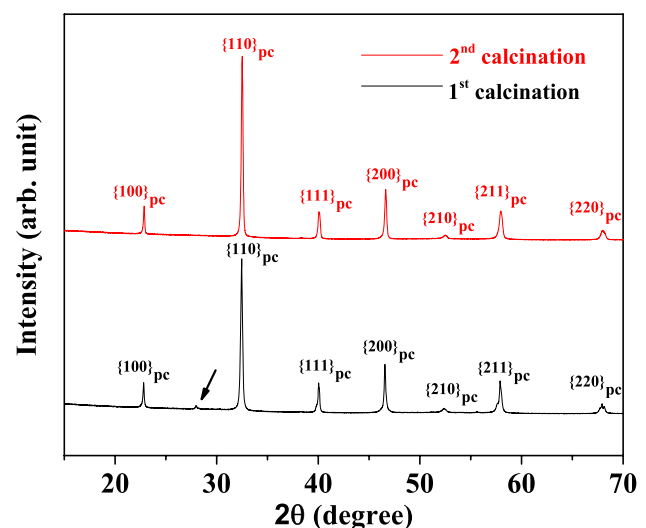


Fig. 1 X-Ray powder diffraction (XRPD) patterns of 5KNN powders after calcining once (1st calcination) and after recalcining (2nd calcination). A peak corresponding to a secondary non perovskite phase is observed at 28° for the one-time calcined powder. The peak disappears after recalcination indicating complete perovskite phase formation

with the calcined powders and they were pelletized by applying uniaxial pressure of 100 MPa. The green pellets were iso-statically pressed at 300 MPa in an incompressible oil medium using a custom made set up. The iso-statically pressed pellets were sintered at 1175 °C for 3 h inside MgO sealed alumina crucibles having spacer powder to minimize the loss of Na, Bi and K. The sintering process was carried out in a muffle furnace (Delta Power, Bangalore, India). The density of the sintered pellets was found to be more than 95% of the theoretical density. The pellets were polished from both sides and were thinned down to 0.5 mm to increase their dielectric breakdown strength [48]. They were electrode by silver painting on both sides for the purpose of electromechanical characterization. Ferroelectric (P-E) hysteresis loops were recorded on the silver painted pellets using a ferroelectric workstation (Radiant Technologies Inc.) having a Sawyer-Tower circuit in an insulating silicone oil medium at varying temperatures by applying an ac electric field having a frequency of 1 Hz. The room temperature and high temperature dielectric measurements were performed on unpoled and poled specimens from a frequency of 10–10<sup>6</sup> Hz using an impedance analyzer (Novocontrol, Montabaur, Germany). The pellets were poled at 120 kV/cm in an insulating silicone oil medium for 1 h using a dc source (IATOME, India). The longitudinal piezoelectric coefficient ( $d_{33}$ ) of the poled pellets was recorded using a Berlincourt meter (Piezotest, PM300) at an applied force of 0.25 N at 110 Hz. The poled pellets were crushed, and the powder obtained is labelled as “poled” powder. Another set of sintered pellets were crushed and annealed at 700 °C for 1 h. The powder thus obtained is labelled as “unpoled” powder. The X-Ray Powder Diffraction (XRPD) of the powders were carried out using a X-Ray Diffractometer (Rigaku, Smartlab, Japan) enabled with a Johanson monochromator in the source arm in the 2 $\theta$  range of 15° to 120° at step size of 0.01° with a scan rate of 1°/min at a power of 4.5 kW in Bragg-Brentano geometry. Compositional analysis was carried out on polished pellets of 0KNN and 5KNN compositions by wavelength dispersive X-ray analysis (WDS) technique using a field emission electron probe microanalyzer (JEOL, JXA-8530F). Scanning electron micrographs (FESEM, Zeiss) of the thermally etched pellets were captured at an accelerating voltage of 20 kV with a spot size of 3 nm and a working distance of 10 mm. Prior to SEM imaging the pellets were gold sputtered for 6 min to avoid charging. The grain size distribution was computed with the aid of the ImageJ software by using the linear intercept method [49]. Detailed structural analysis of the X-Ray powder diffraction (XRPD) data was carried out by Rietveld refinement technique using the Fullprof software package [50].

## 3 Results

### 3.1 Microstructural, structural and compositional studies

The scanning electron micrographs along with the grain size distribution plots of the KNN doped NBT-6BT specimens are shown in Fig. 2. While the grain size of the undoped NBT-6BT i.e. 0KNN composition is 21.3  $\mu\text{m}$ , an abrupt decrease in grain size is observed on doping KNN into the NBT-6BT matrix. 1KNN, 2KNN, 3KNN, 4KNN, 5KNN, 6KNN, 7KNN and 8KNN compositions show grain sizes of 10.3  $\mu\text{m}$ , 8.3  $\mu\text{m}$ , 8.1  $\mu\text{m}$ , 7.5  $\mu\text{m}$ , 7.0  $\mu\text{m}$ , 6.1  $\mu\text{m}$ , 5.8  $\mu\text{m}$  and 5.2  $\mu\text{m}$ , respectively. The grain size and shape are relatively homogeneous with smooth edges, and the microstructure indicates dense ceramic formation as evident from the high density of 95% obtained using the Archimedes liquid displacement method for all the compositions. A microstructure with a homogeneous grain size along with low porosity is very much essential to achieve high dielectric breakdown strength in ferroelectric ceramics, which will make them more useful in energy storage applications [51]. The reduction in grain size on KNN doping can be attributed to the slow diffusion rate of Nb<sup>5+</sup> ion [39, 52]. The sluggish diffusion kinetics of Nb<sup>5+</sup> ion hinders the grain boundary mobility. With increasing KNN doping Nb<sup>5+</sup> concentration also increases in the matrix. The grain boundary migration during synthesis will become slower with increasing Nb<sup>5+</sup> concentration in the matrix. Therefore, grain size gradually decreases with increasing KNN concentration. While the grain size of NBT-6BT (0KNN) reported in the past have been much lower in the range of 2–3  $\mu\text{m}$ , in our case the grain size obtained is 21  $\mu\text{m}$  which is an order of magnitude higher [53–55]. The exponential increase in grain size can be attributed to 0.2 wt% MnO<sub>2</sub> addition to the calcined powder. This played a vital role in enhancing grain growth by aiding matter diffusion through liquid phase sintering process [40, 56, 57]. To determine the effect of MnO<sub>2</sub> doping on grain size, we independently synthesized 0KNN and 5KNN compositions without MnO<sub>2</sub> doping while keeping the synthesis parameters unaltered. The scanning electron micrographs along with the grain size distribution plots for the 0KNN and 5KNN specimens without MnO<sub>2</sub> doping are shown in Fig. 3. While MnO<sub>2</sub> doped 0KNN shows a grain size of 21.3  $\mu\text{m}$  without MnO<sub>2</sub> doping the grain size decreases to 5.6  $\mu\text{m}$ . Similarly, MnO<sub>2</sub> doped 5KNN shows a grain size of 7.0  $\mu\text{m}$  whereas without MnO<sub>2</sub> doping the grain size decreases to 1.6  $\mu\text{m}$ . While MnO<sub>2</sub> doped specimens have grains with smooth edges, the grains without MnO<sub>2</sub> doping have sharp edges. The density



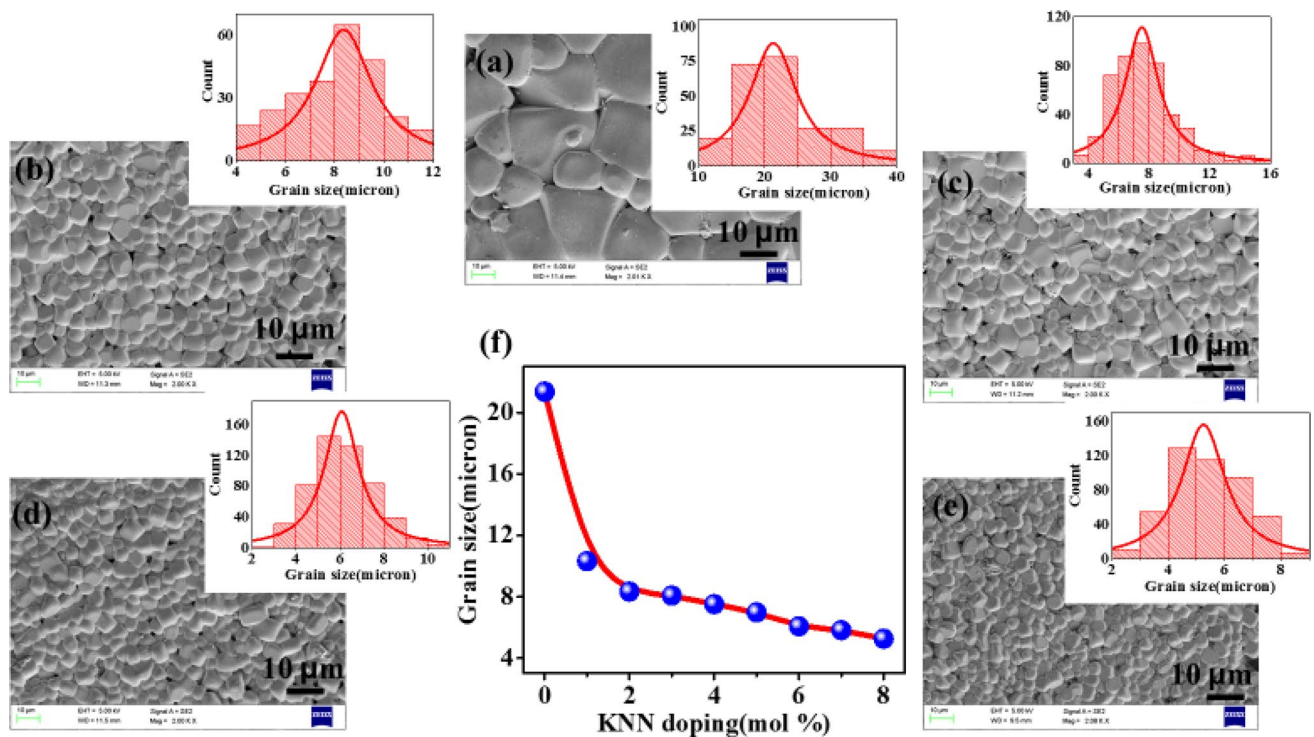


**Fig. 2** Scanning electron micrographs along with the grain size distribution histograms of (a) 0KNN, (b) 2KNN, (c) 4KNN, (d) 6KNN and (e) 8KNN. (f) Shows the variation of grain size of the specimens with

KNN doping. The scale bar is shown in the right hand bottom corner of the micrographs. The red line in (f) is a guide for the eyes

of 0KNN and 5KNN without  $\text{MnO}_2$  doping obtained by using Archimedes liquid displacement method is 92% whereas their  $\text{MnO}_2$  doped counterparts have a density of more than 95%. This indicates that  $\text{MnO}_2$  doping is helpful not only in increasing the grain size but also in densifying the specimen.

The X-ray powder diffraction (XRPD) patterns of the unpoled and poled compositions of the series are shown in Fig. 4. The unpoled compositions from 0KNN to 8KNN show a pseudo-cubic structure as evident from the lack of asymmetry/splitting in the  $\{110\}_{\text{pc}}$ ,  $\{111\}_{\text{pc}}$ ,  $\{200\}_{\text{pc}}$  and  $\{211\}_{\text{pc}}$  Bragg profiles along with the absence of  $\frac{1}{2}\{311\}_{\text{pc}}$  superlattice reflection. While NBT-6BT is known to show a cubic like structure in the undoped state, KNN has an orthorhombic structure ( $Amm2$ ) in the unpoled state [36, 37, 58–62]. It is evident from the cubic like structures of the unpoled specimens that KNN doping into the NBT-6BT matrix in the dilute concentration regime is unable to induce lower symmetry distortion. The XRPD pattern of the unpoled compositions of the series from 0KNN to 8KNN could be accounted for by a  $Pm\bar{3}m$  (cubic) phase structural model (Fig. 5). We observed a gradual increase in lattice parameter on KNN doping with 0KNN showing a lattice parameter of 3.90 Å and 8KNN showing a lattice parameter of 3.91 Å (Fig. 5d). Prior to capturing the XRPD pattern, we adopted the strategy followed by previous

studies. The pellets were manually ground to powder and the obtained powder was annealed at a temperature much higher than the curie temperature in order to remove grinding induced strain [63–65]. Therefore, the pattern observed by us is a genuine structural feature and is not an artifact generated due to grinding induced strain/texture. The poled compositions from 0KNN to 4KNN show visible splitting in the Bragg profiles along with a distinct  $\frac{1}{2}\{311\}_{\text{pc}}$  superlattice reflection. For compositions above 4KNN no visible splitting in the Bragg peaks is observed even in the poled specimens. This indicates that for compositions till 4KNN, application of strong electric field leads to a structural transformation from the high symmetry pseudo-cubic phase to a lower symmetry structure/phase. For compositions above 4KNN the inability of the electric field to force a structural/phase transformation, indicates the dominance of chemical/structural disorder in the ferroelectric matrix [52, 66].

The compositions of  $(0.94-x)\text{NBT}-0.06\text{BT}-x\text{KNN}$  ( $0 \leq x \leq 0.08$ ) series contain Na, Bi and K. These elements are known to be volatile. Their loss during synthesis will determine the final composition of the specimens which in turn will affect the electrical and energy storage properties [67, 68]. Therefore, we decided to measure the weight fraction of the volatile entities through elemental compositional analysis by wavelength-dispersive X-ray

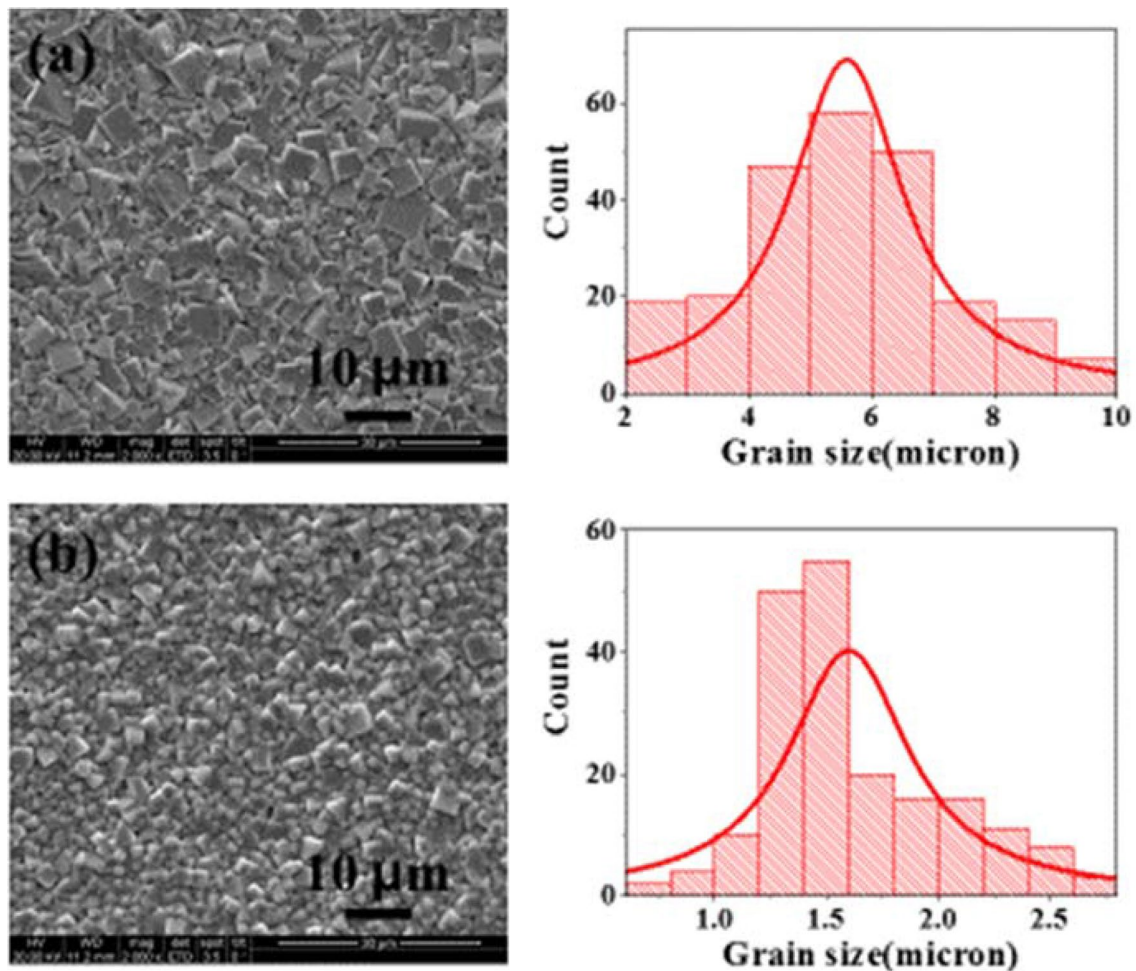


**Fig. 3** Scanning electron micrographs along with the grain size distribution histograms of (a) 0KNN and (b) 5KNN without  $\text{MnO}_2$  doping. The scale bar is shown in the right hand bottom corner of the micrographs

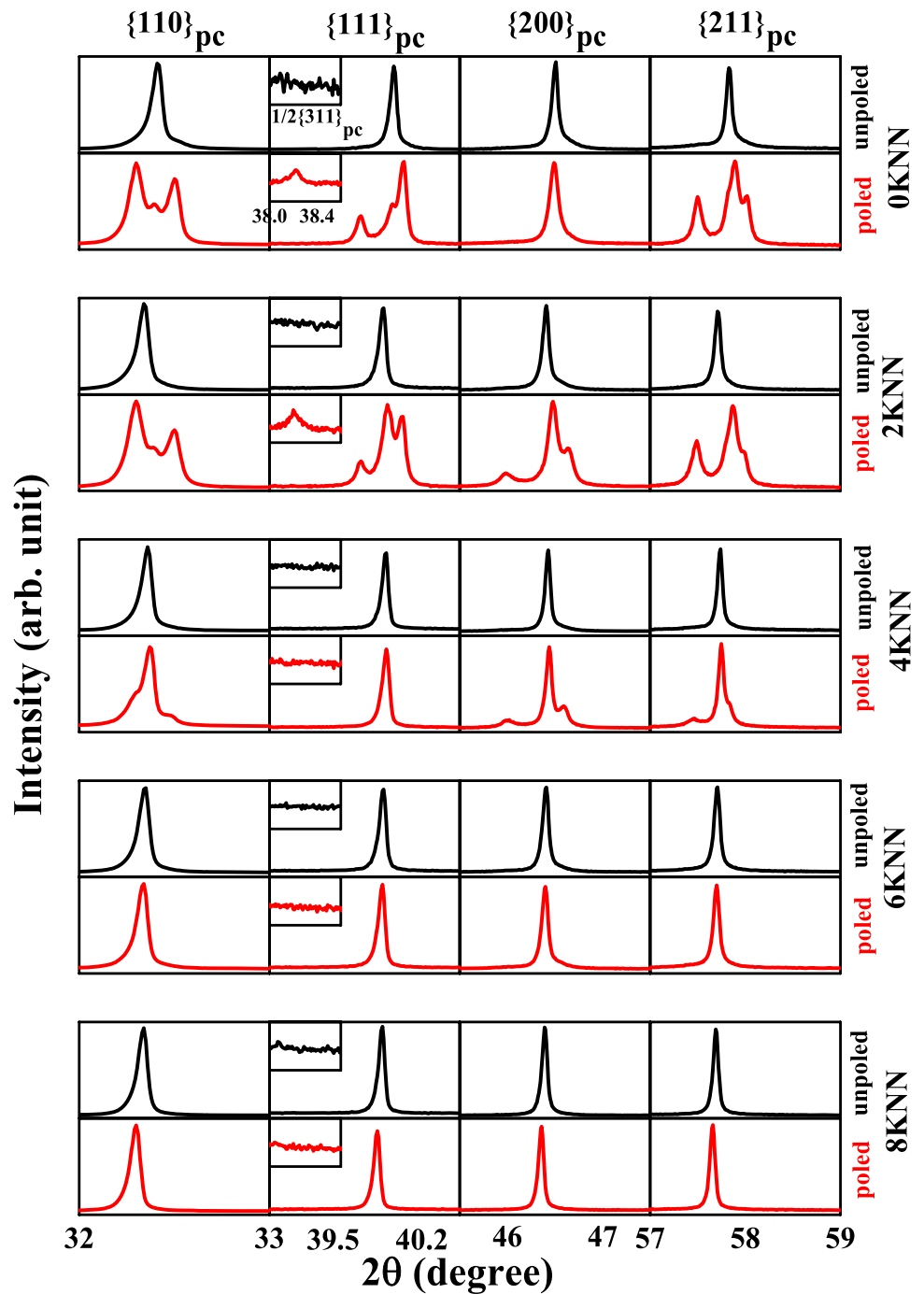
analysis (WDS) techniques. Two representative compositions 0KNN and 5KNN were chosen for this purpose. Determining the atomic weight percentage of Na through WDS was not possible owing to its lower atomic weight of 23u. Bi and K will have a higher loss as compared to Na owing to the comparatively lower melting point of  $\text{Bi}_2\text{O}_3$  (825 °C) and  $\text{K}_2\text{CO}_3$  (900 °C) with respect to  $\text{Na}_2\text{O}$  (1132 °C) [69, 70]. The atomic weight percentage of K in the composition of the series 8KNN with highest K content is less than 0.03%. This is below the resolution limit of WDS and hence it was not possible to determine the concentration of K accurately by WDS for the compositions 0KNN and 5KNN [71, 72]. Therefore, the final analysis was carried out to determine the Bi concentration on 30 randomly chosen points in different grains of the polished pellets of the two specimens. The individual weight percentages of Bi obtained from the experiment for each of the 30 points is plotted in Fig. 6. It is observed that the loss of Bi is within 1% for both 0KNN and 5KNN. The low loss can be attributed to the precautions

taken by us during sample synthesis where the pellets are sintered inside spacer powder compensated MgO sealed alumina crucibles. It is to be noted that the synthesis condition is same for all the compositions of the series. Therefore, the loss of Na/Bi/K is expected to be uniform from all the compositions of the series. This imparts consistency to the results reported by us.

### 3.2 Ferroelectric properties and energy storage density

The ferroelectric (polarization-electric field) hysteresis loops for 0KNN, 4KNN, 5KNN and 8KNN measured at room temperature under a frequency of 1 Hz are shown in Fig. 7. Well saturated ferroelectric loops are observed at an electric field of 70 kV/cm for all the compositions. A systematic reduction in coercive field ( $E_c$ ) is observed with increasing KNN doping. The compositions 0KNN, 4KNN, 5KNN and 8KNN have coercive fields ( $E_c$ ) of 41 kV/

**Fig. 4** Selected X-Ray powder diffraction (XRPD) pseudo-cubic Bragg profiles of compositions with varying KNN doping. The black profiles correspond to unpoled specimens and the red profiles correspond to poled specimens



cm, 24 kV/cm, 17 kV/cm and 16 kV/cm, respectively. The remnant polarization ( $P_r$ ) of 0KNN, 4KNN, 5KNN and 8KNN are  $42 \mu\text{C}/\text{cm}^2$ ,  $12 \mu\text{C}/\text{cm}^2$ ,  $7 \mu\text{C}/\text{cm}^2$  and  $6 \mu\text{C}/\text{cm}^2$ , respectively. Therefore, both coercive field and remnant polarization reduce with increasing KNN content in the NBT-6BT matrix. A recent study by Shi et al. has reported similar findings [73]. This implies that KNN doping results in “domain softening”. Past studies have reported coercive field ( $E_c$ ) of around 27 kV/cm and a remnant polarization ( $P_r$ ) of around  $24 \mu\text{C}/\text{cm}^2$  for the NBT-6BT (0KNN)

composition [74–78]. The enhanced value of coercive field and remnant polarization observed by us in case of 0KNN composition could be due to the minor variation in synthesis procedure and difference in the raw material used. The specimens of the series suffered dielectric breakdown in the range of 75–80 kV/cm. However, for the sake of comparison, we have reported the ferroelectric loops along with their respective energy storage density and discharge efficiency till a field of 70 kV/cm. The energy storage density and discharge efficiency of

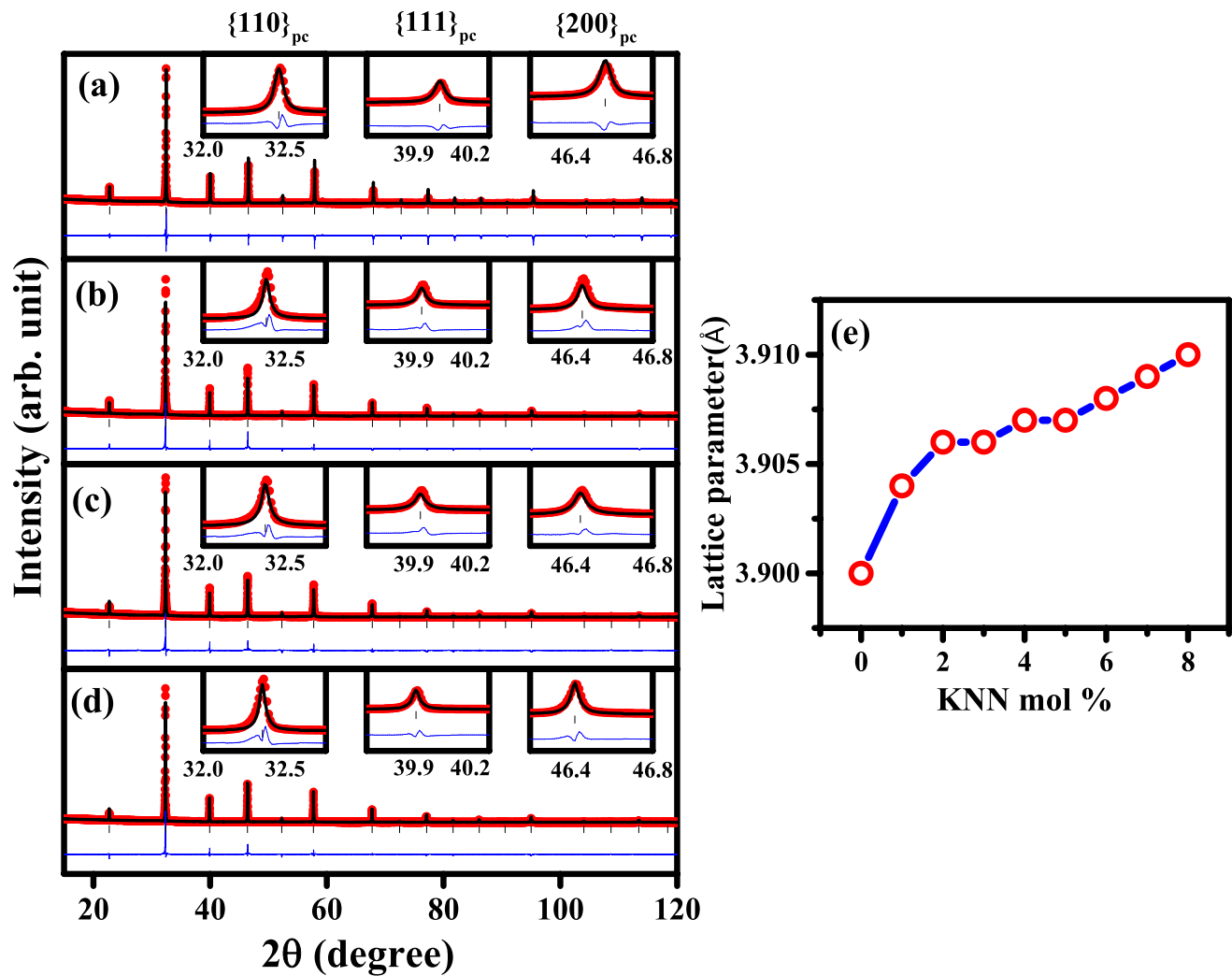


Fig.5 Rietveld fitted XRPD pattern of (a) unpoled 0KNN, (b) unpoled 2KNN, (c) unpoled 4KNN and (d) unpoled 8KNN with  $Pm\bar{3}m$ (cubic) structural model. The insets highlight the magnified plot

of selected Bragg profiles. (e) Variation of lattice parameter of the unit cell with KNN doping

the all the compositions in the series from 0KNN to 8KNN were computed from the ferroelectric hysteresis loop using the following equations. The values obtained are plotted as a function of composition and electric field in Fig. 8.

$$\text{Input energy density } (J_{\text{inp}}) = \int_0^{P_{\text{max}}} EdP \text{ (upon charging)} \tag{1}$$

$$\text{Energy storage density } (J_{\text{store}}) = \int_{P_r}^{P_{\text{max}}} EdP \text{ (upon discharging)} \tag{2}$$

$$\text{Discharge efficiency } (\eta) = \frac{J_{\text{store}}}{J_{\text{inp}}} * 100\% \tag{3}$$

In the above equations  $J_{\text{inp}}$  is the energy supplied to the material(input energy density),  $J_{\text{store}}$  is the energy stored in the material(energy storage density),  $P$  is polarization,  $P_{\text{max}}$  is the maximum polarization,  $P_r$  is the remanent polarization,  $E$  is the amplitude of the applied electric field and  $\eta$  is efficiency of the material(discharge efficiency).

0KNN, 1KNN, 2KNN and 3KNN have energy storage densities of 0.08 J/cm<sup>3</sup>, 0.17 J/cm<sup>3</sup>, 0.22 J/cm<sup>3</sup> and 0.35 J/cm<sup>3</sup> respectively at a field of 70 kV/cm. 0KNN, 1KNN, 2KNN and 3KNN have discharge efficiencies of 3%, 6%, 10% and 18% respectively at a field of 70 kV/cm. Therefore, the energy storage density ( $J_{\text{store}}$ ) and the discharge efficiency( $\eta$ ) of the compositions show gradual improvement upto 3 mol% KNN doping. 4KNN has an energy storage density of 0.77 J/cm<sup>3</sup> and a discharge efficiency of 41% which is



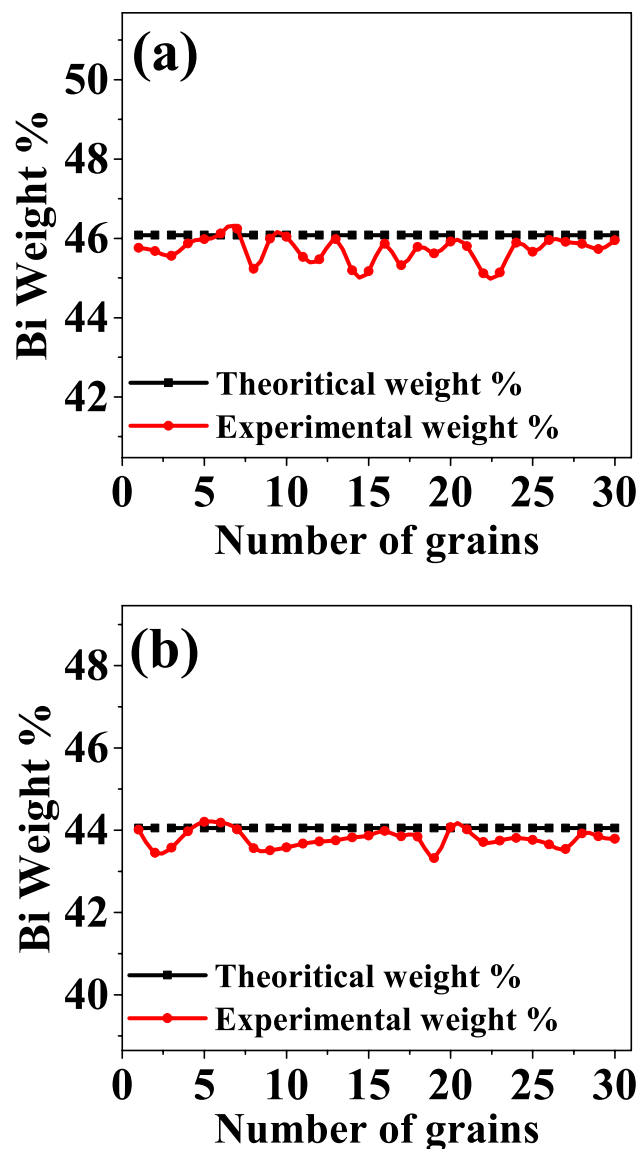


**Fig. 6** Variation of Bi weight percentage obtained from wavelength dispersive x-ray (WDS) analysis of 30 arbitrarily selected points in different grains of the polished 0KNN and 5KNN pellets. It is observed that the loss of Bi is less than 1%

significantly better than that of 3KNN. On further increasing the KNN doping the improvement in energy storage and discharge efficiency is quite drastic with 5KNN having an energy storage density of  $1.19 \text{ J/cm}^3$  and a discharge efficiency of 60%. Beyond 5 mol% KNN doping both energy density and discharge efficiency saturate/stabilize with 6KNN, 7KNN and 8KNN having energy storage densities of  $1.18 \text{ J/cm}^3$ ,  $1.17 \text{ J/cm}^3$  and  $1.14 \text{ J/cm}^3$  respectively along with discharge efficiencies of 60%, 58% and 59% respectively (Fig. 8a and b). We also measured the energy storage density and discharge efficiencies of the compositions 4KNN, 5KNN and 8KNN as a function of electric field

(Fig. 8c and d). Energy storage density of 4KNN is  $0.25 \text{ J/cm}^3$  at 40 kV/cm,  $0.39 \text{ J/cm}^3$  at 50 kV/cm,  $0.56 \text{ J/cm}^3$  at 60 kV/cm and  $0.77 \text{ J/cm}^3$  at 70 kV/cm. For 5KNN energy storage density is  $0.39 \text{ J/cm}^3$  at 40 kV/cm,  $0.61 \text{ J/cm}^3$  at 50 kV/cm,  $0.88 \text{ J/cm}^3$  at 60 kV/cm and  $1.19 \text{ J/cm}^3$  at 70 kV/cm. Similarly, for 8KNN energy storage density is  $0.37 \text{ J/cm}^3$  at 40 kV/cm,  $0.58 \text{ J/cm}^3$  at 50 kV/cm,  $0.84 \text{ J/cm}^3$  at 60 kV/cm and  $1.14 \text{ J/cm}^3$  at 70 kV/cm. Discharge efficiency of 4KNN is 41% at 40 kV/cm, 42% at 50 kV/cm, 43% at 60 kV/cm and 41% at 70 kV/cm. For 5KNN discharge efficiency remains unchanged at 60% at fields of 40 kV/cm, 50 kV/cm, 60 kV/cm and 70 kV/cm. Similarly, for 8KNN discharge efficiency is 57% at 40 kV/cm, 56% at 50 kV/cm, 58% at 60 kV/cm and 59% at 70 kV/cm. It can be clearly seen from the above trends that while the energy storage density shows a linear increase with the increase in amplitude of the ac electric field, in contrast the discharge efficiency largely remains unaffected by the amplitude of the ac electric field.

To ascertain the upper working limit of the compositions, we measured the ferroelectric loops for the compositions 0KNN and 5KNN as a function of temperature as shown in Fig. 9(a and b). It is observed that the loops become slimmer with increasing temperature indicating the ease of domain mobility at higher temperature owing to thermal agitation [15]. The coercive field of 0KNN at 30 °C is 41 kV/cm which reduces to 27 kV/cm at 75 °C and 21 kV/cm at 100 °C. The energy storage density shows minor improvement from  $0.08 \text{ J/cm}^3$  at 30 °C to  $0.09 \text{ J/cm}^3$  at 75 °C and  $0.10 \text{ J/cm}^3$  at 100 °C (Fig. 9c). The discharge efficiency shows an enhancement from 3% at 30 °C to 5% at 75 °C and 7% at 100 °C (Fig. 9d). Similarly, in the case of 5KNN the coercive field which was initially 17 kV/cm at 30 °C, reduced to 12 kV/cm at 75 °C and 100 °C. This results in the enhancement of energy storage density from  $1.18 \text{ J/cm}^3$  at 30 °C to  $1.24 \text{ J/cm}^3$  at 75 °C and  $1.26 \text{ J/cm}^3$  at 100 °C (Fig. 9c). The discharge efficiency also improves from 60% at 30 °C to 61% at 75 and 62% at 100 °C (Fig. 9c). It was not possible to measure beyond 100 °C as both the compositions suffered dielectric breakdown presumably due to thermally induced leakage current. Therefore, the upper working limit of the composition 0KNN is 100 °C.

We have synthesized all the compositions of the series with 0.2 wt%  $\text{MnO}_2$  additive. It was done with an objective of reducing leakage current and enhancing densification of the samples. However, for the sake of comparison, we have also carried out ferroelectric hysteresis study on independently synthesized 0KNN and 5KNN compositions without  $\text{MnO}_2$  doping. The ferroelectric hysteresis and leakage current loops of 0KNN and 5KNN compositions with and without  $\text{MnO}_2$  doping are shown in Fig. 10. There is a minor improvement in ferroelectric hysteresis and leakage current characteristics of 0KNN with  $\text{MnO}_2$  doping.



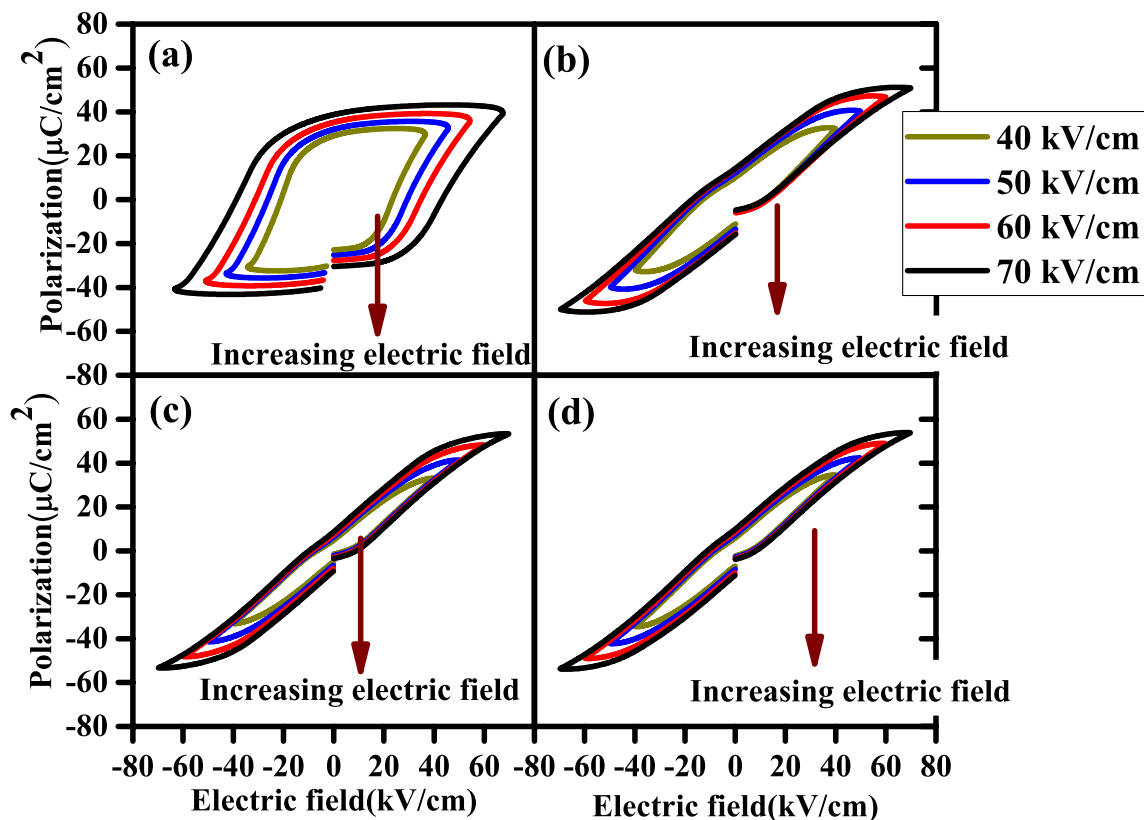


**Fig. 7** Ferroelectric(P-E) hysteresis loops of (a) 0KNN, (b) 4KNN, (c) 5KNN and (d) 8KNN at varying electric fields. The measurements were carried out at a frequency of 1 Hz at room temperature. The numbers shown in frame (b) indicate the amplitude of the ac electric field

While 0KNN compositions without  $\text{MnO}_2$  doping has a  $P_r$  of  $30 \mu\text{C}/\text{cm}^2$ , the value of  $P_r$  increases to  $38 \mu\text{C}/\text{cm}^2$  with  $\text{MnO}_2$  doping. The coercive field of 0KNN decreases with  $\text{MnO}_2$  doping from  $34 \text{ kV}/\text{cm}$  to  $32 \text{ kV}/\text{cm}$  (Fig. 10a). The average values of the leakage current maxima is  $1.30 \text{ mA}/\text{cm}^2$  for 0KNN with  $\text{MnO}_2$  doping and  $1.33 \text{ mA}/\text{cm}^2$  for 0KNN without  $\text{MnO}_2$  doping (Fig. 10b). However,  $\text{MnO}_2$  doping has a drastic effect on ferroelectric hysteresis and leakage current characteristics of 5KNN. While 5KNN with  $\text{MnO}_2$  doping yields a proper ferroelectric hysteresis loop, the loop of 5KNN without  $\text{MnO}_2$  doping resembles that of a lossy dielectric (Fig. 10c). This is due to the high leakage current maxima of  $1.87 \text{ mA}/\text{cm}^2$  obtained in 5KNN without  $\text{MnO}_2$  doping (Fig. 10d). The maximum value of leakage current reduces to  $0.84 \text{ mA}/\text{cm}^2$  for 5KNN with  $\text{MnO}_2$  doping. This implies that  $\text{MnO}_2$  doping is essential for compositions containing  $\text{K}_{0.5}\text{Na}_{0.5}\text{NbO}_3$  (KNN) to obtain a proper ferroelectric hysteresis loop by reducing the leakage current.

### 3.3 Dielectric properties and relaxor behavior

The temperature dependent dielectric permittivity plots of 0KNN and 5KNN both in unpoled and poled states are

shown in Fig. 11. The permittivity vs temperature plots of 0KNN and 5KNN have two shoulder in both unpoled and poled states. The shoulder at lower temperature observed at around  $150^\circ\text{C}$  is attributed to ferroelectric to antiferroelectric phase transition and the shoulder at higher temperature of about  $300^\circ\text{C}$  is assigned to anti-ferroelectric to paraelectric phase transition [43, 44]. The shoulder at around  $150^\circ\text{C}$  is frequency dependent which is a characteristic of relaxor ferroelectrics [27, 59]. A sharp but weak anomaly at  $T_d = 60^\circ\text{C}$  is seen in poled 0KNN (Fig. 11b). However, this anomaly is not observed in the unpoled 0KNN (Fig. 11a). Interestingly it is also not seen in poled 5KNN (Fig. 11d). In XRPD studies we observe that poling stabilizes a lower symmetry ferroelectric phase for 0KNN however 5KNN retains its cubiclike structure even after poling. Therefore, the anomaly observed at  $60^\circ\text{C}$  for poled 0KNN could be related to the transformation of the field stabilized ferroelectric phase to the higher symmetry cubiclike phase. This temperature is also commonly known as depolarization temperature [53, 66].

The dielectric dispersion (permittivity vs  $\ln$  frequency) plots for unpoled and poled specimens of 0KNN, 2KNN and 8KNN are shown in Fig. 12(a–c). Past studies have interpreted the slope of the linear part of the dielectric

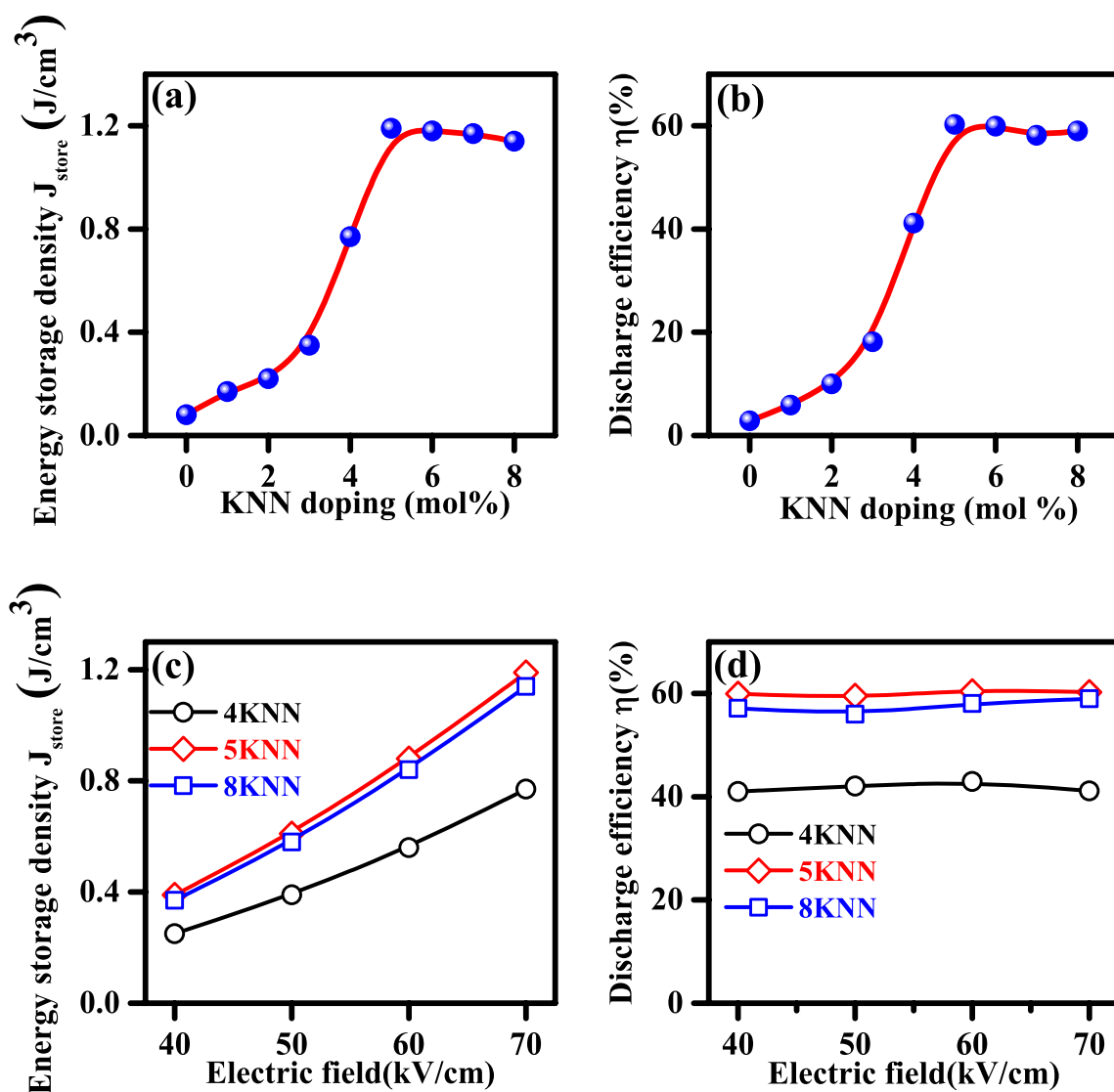


**Fig. 8** (a) Energy density and (b) Discharge efficiency of the compositions with varying KNN doping at an electric field of 70 kV/cm with at a frequency of 1 Hz. (c) Energy density and (d) Discharge

efficiency of selected compositions as a function of electric field. The measurements were carried out at room temperature. The red line in (a & b) is a guide for the eyes

dispersion plot as a quantitative measure of the structural/chemical disorder existing in the ferroelectric matrix [63, 79–83]. In this study also we have considered the slope of the  $\epsilon'$  vs  $\ln f$  plot as a quantitative measure of the structural/chemical disorder prevalent in the ferroelectric matrix. In Fig. 12d the variation of slopes of the dielectric dispersion plots of the unpoled and poled compositions as a function of KNN doping is shown. The slope of unpoled 0KNN, 1KNN, 2KNN, 3KNN, 4KNN, 5KNN, 6KNN, 7KNN and 8KNN is  $-93, -98, -106, -114, -124, -162, -169, -170$  and  $-178$  respectively. The slope of poled 0KNN, 1KNN, 2KNN, 3KNN, 4KNN, 5KNN, 6KNN, 7KNN and 8KNN is  $-36, -42, -53, -73, -94, -156, -164, -166$  and  $-176$  respectively. It is observed that KNN doping increases the slope

of both unpoled and poled compositions which indicates that KNN doping into the NBT-6BT matrix increases the structural heterogeneity/disorder both in the unpoled and poled specimens. When KNN doping is more than 4 mol%, even strong electric field is ineffective in reducing the slope/disorder indicating the dominance of disorder in the ferroelectric matrix.

### 3.4 Piezoresponse and disorder

The longitudinal piezoelectric response ( $d_{33}$ ) of the compositions as a function of KNN doping is shown in Fig. 13a. In the dilute KNN doping regime a high longitudinal piezoelectric response ( $d_{33}$ ) is obtained. 0KNN, 1KNN, 2KNN and

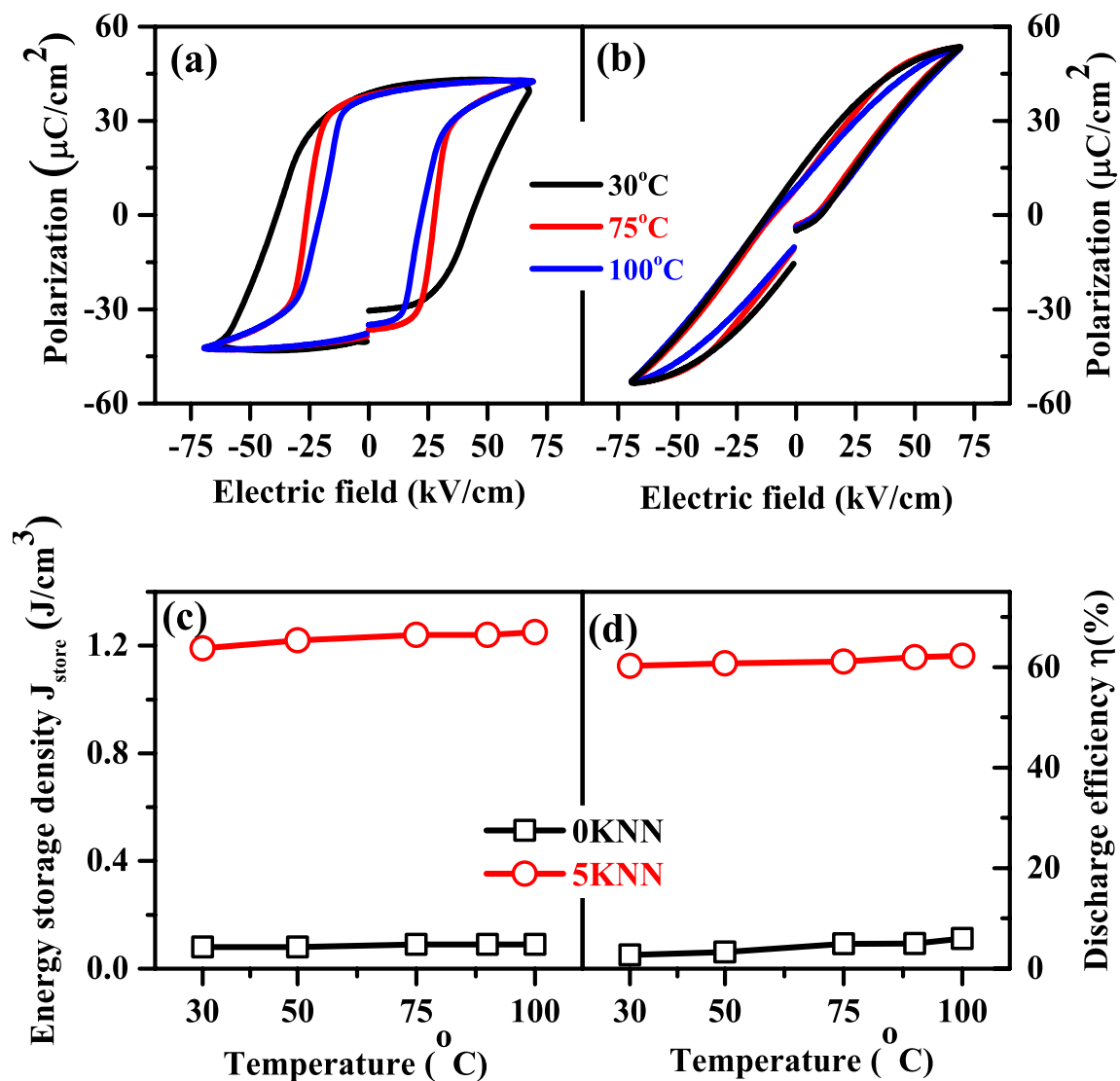


**Fig. 9** Ferroelectric(P-E) hysteresis loops of (a) 0KNN and (b) 5KNN at temperatures of 30 °C, 75 °C and 100 °C measured with an ac electric field of 70 kV/cm. The frequency of the ac electric field is 1 Hz.

(c) Energy density and (d) Discharge efficiencies of 0KNN and 5KNN as a function of temperature

3KNN show  $d_{33}$  values of 151 pC/N, 134 pC/N, 126 pC/N and 117 pC/N respectively. On further increasing KNN doping in the NBT-6BT matrix there is a noticeable decay in piezoresponse. A drastic drop in  $d_{33}$  value from 117 pC/N for 3KNN to 78 pC/N for 4KNN is observed. There is a further drop in  $d_{33}$  to 23 pC/N for 5KNN, 17 pC/N for 6KNN, 12 pC/N for 7KNN and 4 pC/N for 8KNN. We observe in XRPD studies and dielectric dispersion studies that when KNN doping is more than 4 mol%, electric field is unable to overcome the structural heterogeneity/disorder present in the matrix. In XRPD studies this is observable from the characteristic of the Bragg peaks for compositions above 4KNN, where the singlet shape of the Bragg peaks is retained even after the application of strong electric field.

In dielectric dispersion studies it is seen that the slope ( $\epsilon' \text{ vs } \ln f$ ) does not undergo significant change even after poling for compositions beyond 4KNN. Above observations indicate that for specimens with more than 4 mol% KNN doping, long-range ferroelectric order is not formed on application of electric field. This leads to a drastic decrease in piezoresponse ( $d_{33}$ ). Figure 13b shows the variation in  $d_{33}$  with the "degree of ordering" ( $\Delta s$ ). "Degree of ordering" is quantitative measurement of the effectiveness of electric field in inducing long range ordering in the ferroelectric matrix [79, 80]. Mathematically "degree of ordering" ( $\Delta s$ ) is calculating by subtracting the slope of the unpoled specimen obtained from dielectric dispersion plot from that of the poled specimen (Fig. 12d).  $\Delta s$  for 0KNN, 1KNN, 2KNN,

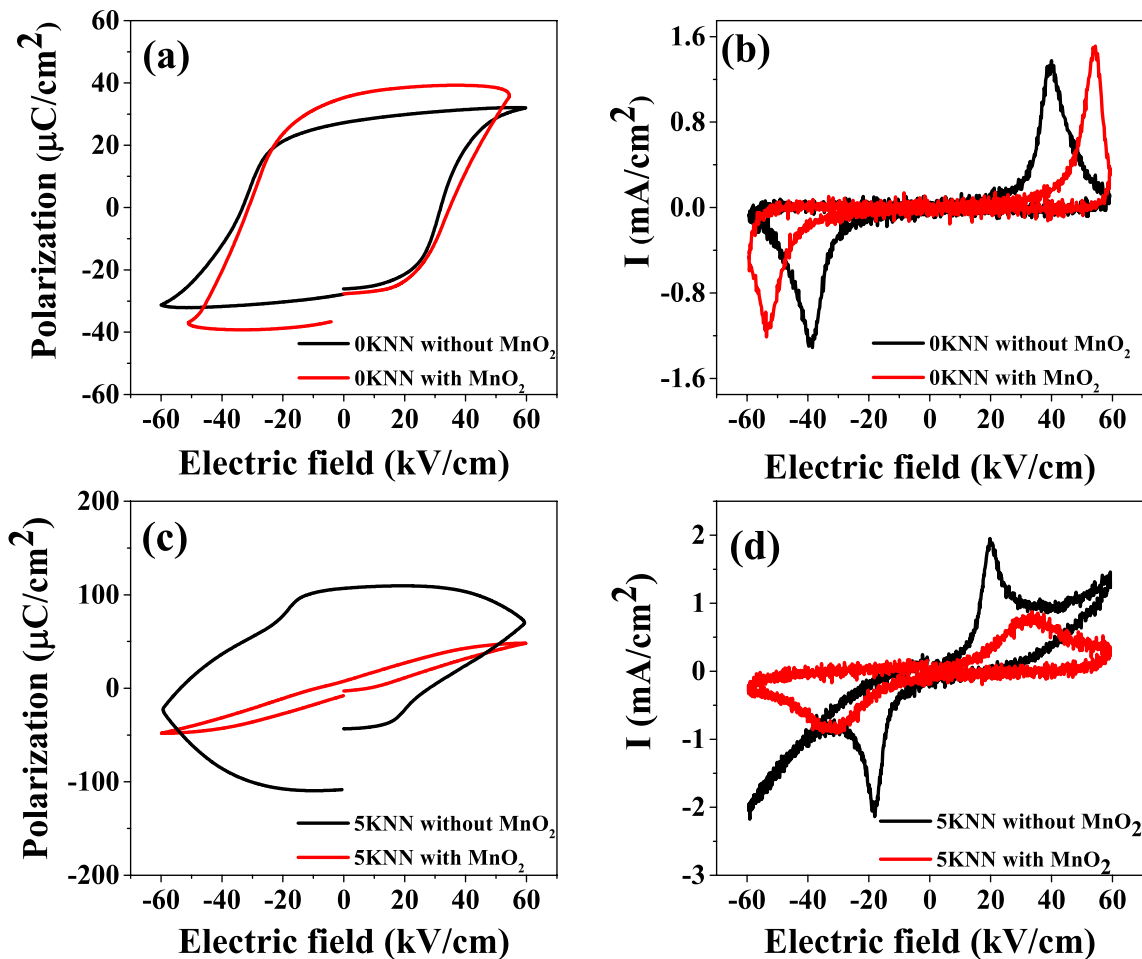


**Fig. 10** (a) Polarization (P)—Electric field (E)(ferroelectric) and (b) Leakage current(I)—Electric field(E) plot for 0KNN specimen with and without MnO<sub>2</sub> doping. (c) Polarization (P)—Electric field (E)(fer-

roelectric) and (d) Leakage current(I)—Electric field(E) plot for 5KNN specimen with and without MnO<sub>2</sub> doping. All the measurements were carried out at room temperature

3KNN, 4KNN, 5KNN, 6KNN, 7KNN and 8KNN is 57, 56, 54, 41, 30, 5, 5, 4 and 3 respectively. We observe that the composition 0KNN showing the maximum “degree of ordering” ( $\Delta s \sim 57$ ) has the highest piezoresponse ( $d_{33} \sim 151$  pC/N). This implies that irrespective of the structural heterogeneity/disorder initially present in the ferroelectric matrix, the specimen in which applied electric field is most effective in reducing the inherent polar-structural heterogeneity/disorder and establishing long range ferroelectric order will show the highest piezoresponse. We observe that while disorder increases with KNN content, the coercive field ( $E_c$ ), remnant polarization ( $P_r$ ) and piezoresponse ( $d_{33}$ ) decreases. This indicates that presence of disorder makes domains softer i.e. they easily align on application of electric field and easily randomize when the field is withdrawn. A low coercive field and low remnant polarization ensures a high value of energy storage density and discharge efficiency. Therefore, energy storage density increases with disorder.

#### 4 Discussion

Energy storage density and discharge efficiency of polycrystalline ceramics have been vigorously investigated for relaxor and antiferroelectric materials. From our study it is evident that while disorder (quantitatively measured from the slope of the dielectric dispersion plot) is helpful in improving the energy storage properties, it has a detrimental effect on the piezoresponse. Therefore, energy storage density and piezoresponse are complimentary properties i.e. one grows at the expense of other. The composition 5KNN which has low piezoresponse value of 23 pC/N shows the highest energy density of 1.19 J/cm<sup>3</sup> and a discharge efficiency of 60% at a field of 70 kV/cm. Gao et al. and Chandrasekhar et al. had reported energy storage densities of 0.59 J/cm<sup>3</sup> and 0.5 J/cm<sup>3</sup> for the composition 5KNN at an electric field of 60 kV/cm [43, 44]. The higher energy storage density obtained by us as compared to prior reported values could be due to the higher dielectric



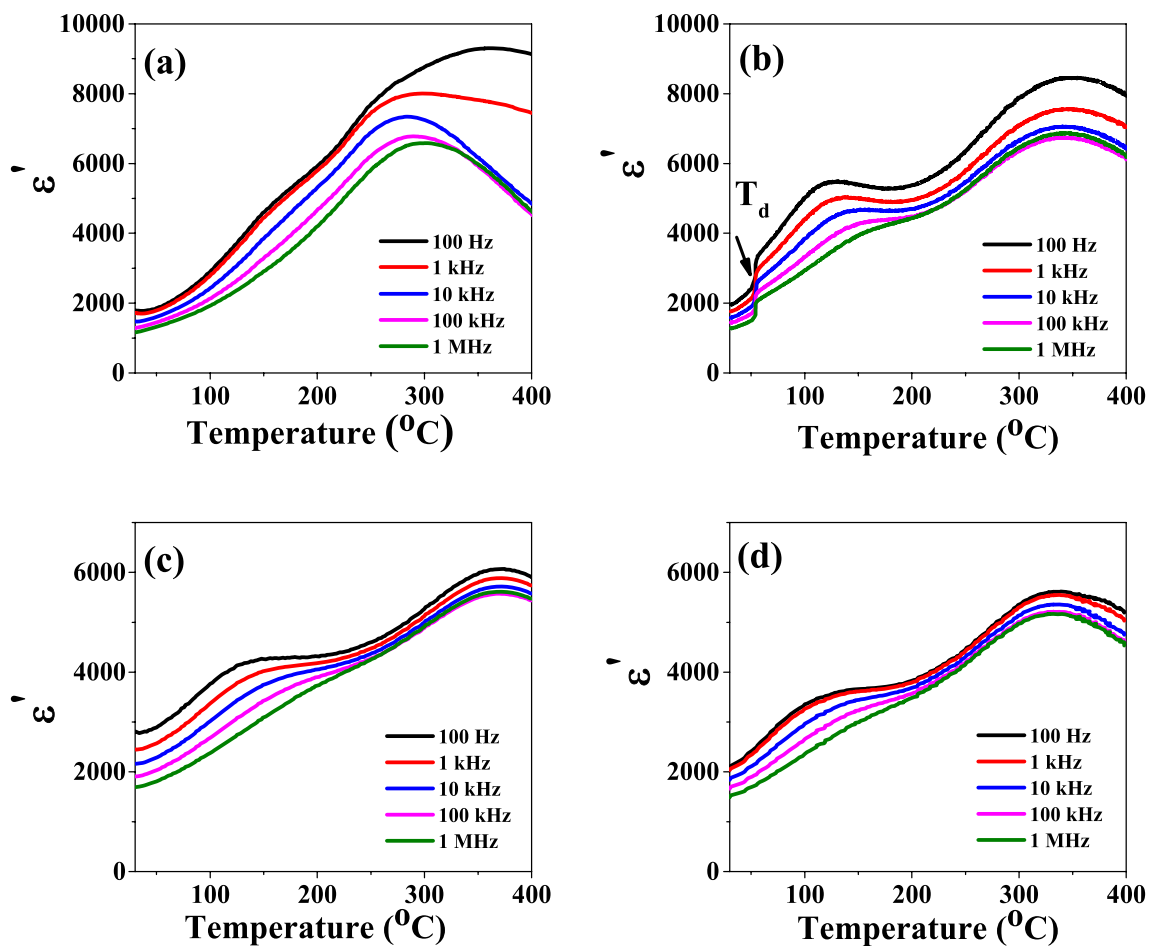


**Fig. 11** Temperature dependent dielectric permittivity plots of (a) 0KNN unpoled, (b) 0KNN poled, (c) 5KNN unpoled and (d) 5KNN poled specimens measured at frequencies of 100 Hz, 1 kHz, 10 kHz, 100 kHz and 1 MHz

breakdown strength of our sample achieved through densification by  $\text{MnO}_2$  doping. In fact, the energy storage density of  $1.19 \text{ J/cm}^3$  obtained by us for the 5KNN composition is even better than the value of  $0.90 \text{ J/cm}^3$  reported for 5KNN two step sintered samples by Ding et al. [45]. This suggests that  $\text{MnO}_2$  doping is a better way to enhance the energy storage efficiency of a material as compared to two step sintering. The value obtained by us is superior to that of some recently reported NBT based lead free systems. Chandrasekhar et al. reported an energy storage density of  $0.28 \text{ J/cm}^3$  and a discharge efficiency of 47% in  $0.84(0.93\text{Na}_{0.5}\text{Bi}_{0.5}\text{TiO}_3-0.07\text{K}_{0.5}\text{Na}_{0.5}\text{NbO}_3)-0.16\text{NaNbO}_3$  ceramics under an electric field of  $65 \text{ kV/cm}$  [84]. Ren et al. reported an energy storage density of  $0.84 \text{ J/cm}^3$  and a discharge efficiency of 48% in  $0.15(0.91\text{Na}_{0.5}\text{Bi}_{0.5}\text{TiO}_3-0.09\text{BiAlO}_3)-0.15\text{SrTiO}_3$  under an electric field of  $90 \text{ kV/cm}$  [85]. However, there exists quite a few reports on lead free ferroelectric systems which have superior energy storage properties in comparison to our system. These lead-free ferroelectric systems are summarized in Table 1. We observe

that the energy storage density of these systems has been measured at a higher electric field in comparison to our field value of  $70 \text{ kV/cm}$ . We were not able to measure the energy storage properties at higher field strength because our system suffered dielectric breakdown at a field of  $75 \text{ kV/cm}$ . To overcome this drawback, we can increase the dielectric breakdown strength of our material by further densifying it using Spark Plasma Sintering (SPS) technique and fabricating multi-layer structure. It will enable us to achieve a very high value of energy density which will make our material a strong candidate for industrial applications. The composition 0KNN having the lowest disorder in unpoled and poled states has the highest piezoresponse of  $151 \text{ pC/N}$ . It shows the lowest energy density of  $0.08 \text{ J/cm}^3$  and a discharge efficiency of 3%. This indicates that to obtain a high value of energy storage density, disorder needs to be induced in the ferroelectric matrix. In our case it is induced by the doping of KNN into the NBT-6BT matrix which breaks the long-range ferroelectric ordering. However, the enhanced disorder which is helpful in improving

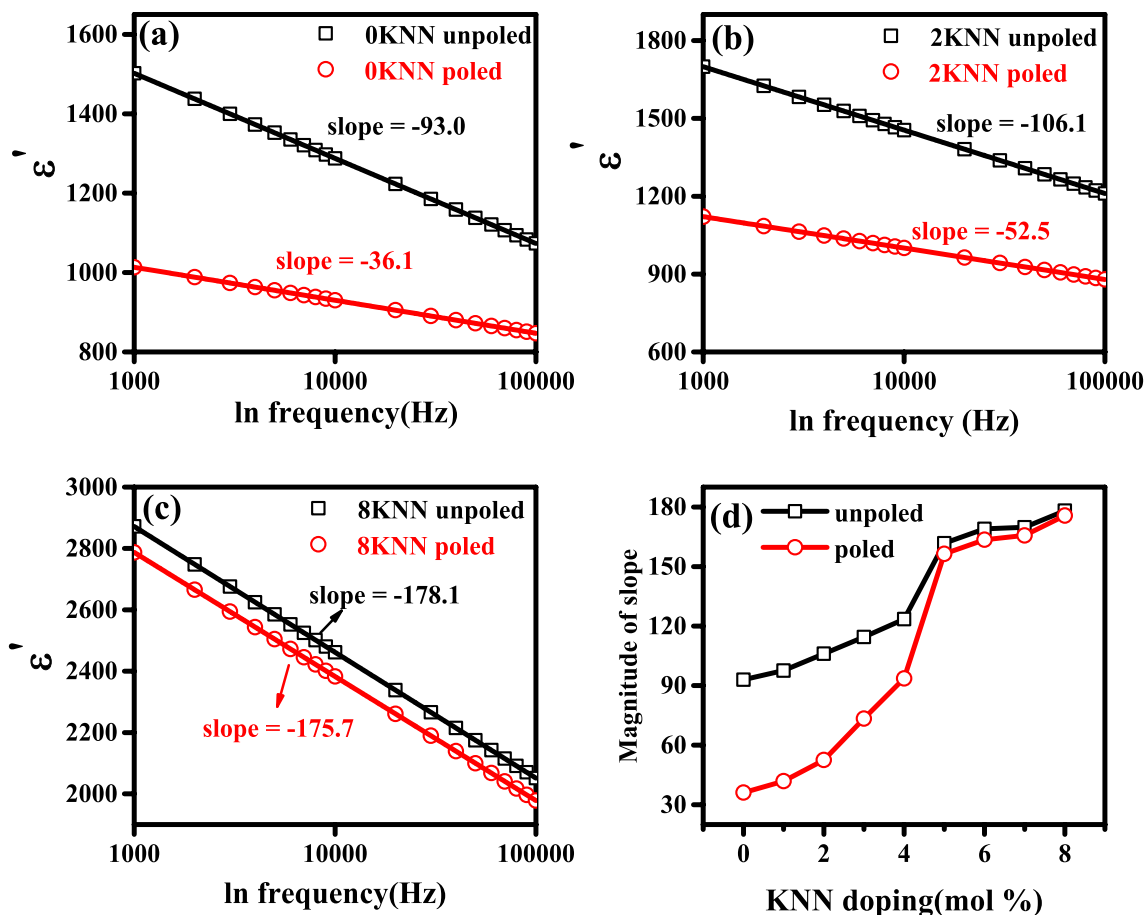


Fig. 12 Dielectric dispersion (permittivity vs ln frequency) plots of unpoled (black) and poled (red) (a) 0KNN, (b) 2KNN and (c) 8KNN compositions at room temperature. (d) Variation in magnitude of

slope obtained from the dielectric dispersion (permittivity vs ln frequency) plots for unpoled and poled specimens with KNN doping

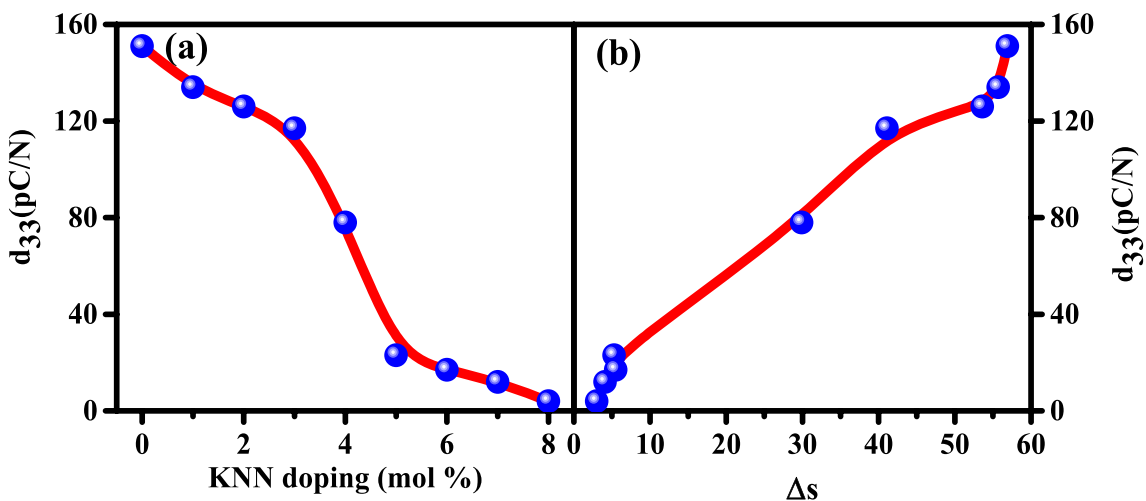


Fig. 13 (a) Variation of longitudinal piezoelectric coefficient ( $d_{33}$ ) with KNN doping. (b) Variation of longitudinal piezoelectric coefficient ( $d_{33}$ ) with degree of ordering ( $\Delta s$ ). The red line in (a & b) is a guide for the eyes

**Table 1** Lead free ferroelectric ceramics showing superior energy storage properties in comparison to 0.2 wt% MnO<sub>2</sub> doped 0.89NBT-0.06BT-0.05KNN

Compound	E (kV/cm)	W (J/cm <sup>3</sup> )	η (%)	Reference
BT-BMT	340	4.49	93	[86]
BF-BT-NN	360	8.12	90	[87]
BNT-BLZT/STL	294	2.72	74	[88]
NBT-BS/BZ	245	2.08	89	[89]
BNBT-BSN	115	1.2	87	[90]
BBNLTZ	136	1.55	73	[91]
BNT-ST-AN/SiO <sub>2</sub>	316	3.22	85	[92]
NBTBLT-KNN	90	1.1	80	[93]
BMT-BT	240	1.89	83	[94]
BT-NBT-SYN	152	1.36	74	[95]
BT-BNN	200	2.09	96	[96]
BT-KBN	180	2.51	87	[97]
BNT-ST-AN	120	2.03	61	[98]
BT-BZNT	1047	10.12	89	[99]
NBT-BT-BF	80	1.4	90	[15]
0.89NBT-0.06BT-0.05KNN/MnO <sub>2</sub>	70	1.19	60	This work

the energy storage property and discharge efficiency of ferroelectric ceramics proves detrimental for the piezoresponse. Therefore, our work is also significant from the fundamental viewpoint as we prove that energy storage density and piezoresponse are complimentary properties which grow at the expense of each other.

## 5 Conclusions

(0.94-x)Na<sub>0.5</sub>Bi<sub>0.5</sub>TiO<sub>3</sub>-0.06BaTiO<sub>3</sub>-xK<sub>0.5</sub>Na<sub>0.5</sub>NbO<sub>3</sub> (0 ≤ x ≤ 0.08) ceramics were prepared by the conventional solid-state ceramic synthesis route. It is observed that the grain size of the ceramics decreases with increasing KNN addition from 21.3 μm for 0KNN to 5.2 μm for 8KNN. While the structure of the unpoled ceramics is cubic like, for compositions upto 4KNN application of electric field/poling results in a lower symmetry structure. For compositions beyond 4KNN the poled structure is also cubic like. The energy storage density increases from 0.08 J/cm<sup>3</sup> for 0KNN to 1.19 J/cm<sup>3</sup> for 5KNN and saturates/stabilizes thereafter. Discharge efficiency also follows a similar trend and increases from 3% for 0KNN to 60% for 5KNN. The piezoresponse decreases upon KNN doping from 151 pC/N for 0KNN to 4 pC/N for 8KNN. The disorder in the ferroelectric matrix increases upon KNN doping in both unpoled and poled states. Presence of disorder in the ferroelectric matrix enhances the energy storage density and discharge efficiency but proves detrimental for the piezoresponse.

**Acknowledgements** Rajeev Ranjan thanks the Science and Engineering Research Board (SERB) of the Department of Science and Technology, Govt. of India for financial support (Grant No. EMR/2016/001457). Arnab De acknowledges DST, Govt of India for Inspire fellowship.

## Compliance with ethical standards

**Conflict of interest** The authors declare no conflict of interest.

## References

- Davis GR (1990) Energy for planet earth. *Sci Am* 263(3):54–63
- Kamat PV (2013) Energy outlook for planet Earth. *J Phys Chem Lett* 4(10):1727–1729. <https://doi.org/10.1021/jz400902s>
- Keyes RW (1988) Miniaturization of electronics and its limits. *IBM J Res Dev* 32(1):84–88
- Borkar H, Singh VN, Singh BP, Tomar M, Gupta V, Kumar A (2014) Room temperature lead-free relaxor-antiferroelectric electroceramics for energy storage applications. *RSC Adv* 4(44):22840–22847. <https://doi.org/10.1039/c4ra00094c>
- Peng B, Zhang Q, Li X et al (2015) Large energy storage density and high thermal stability in a highly textured (111)-oriented Pb<sub>0.8</sub>Ba<sub>0.2</sub>ZrO<sub>3</sub> relaxor thin film with the coexistence of antiferroelectric and ferroelectric phases. *ACS Appl Mater Inter* 7(24):13512–13517. <https://doi.org/10.1021/acsami.5b02790>
- Hao X (2013) A review on the dielectric materials for high energy-storage application. *J Adv Dielec* 3(01):1330001
- Dan Y, Xu H, Zou K et al (2018) Energy storage characteristics of (Pb,La)(Zr,Sn,Ti)O<sub>3</sub> antiferroelectric ceramics with high Sn content. *Appl Phys Lett* 113(6):063902. <https://doi.org/10.1063/1.5044712>
- Feng Y, Xu Z, Li H, Yao X (2004) Effect of La modifier on the electric hysteresis of lead zirconate stannate titanate compounds. *Ceram Int* 30(7):1393–1396. <https://doi.org/10.1016/j.ceramint.2003.12.089>
- Parui J, Krupanidhi SB (2008) Enhancement of charge and energy storage in sol-gel derived pure and La-modified PbZrO<sub>3</sub> thin films. *Appl Phys Lett* 92(19):192901. <https://doi.org/10.1063/1.2928230>
- EU-Commission Directive 2013/28/EU of 17 May 2013 amending annex II to directive 2000/53/EC of the European Parliament and of the Council on end-of-life vehicles. *Off J Eur Union* 2013; L135:14–8
- EU-Council Directive 89/677/EEC of 21 December 1989 amending for the eighth time Directive 76/769/EEC on the approximation of the laws, regulations and administrative provisions of the member states relating to restrictions on the marketing and use of certain dangerous substances and preparations. *Off J Eur Commun* 1989; L398: 19–23
- Rödel J, Jo W, Seifert KTP, Anton EM, Granzow T, Damjanovic D (2009) Perspective on the development of lead-free piezoceramics. *J Am Ceram Soc* 92(6):1153–1177. <https://doi.org/10.1111/j.1551-2916.2009.03061.x>
- Rödel J, Li JF (2018) Lead-free piezoceramics: status and perspectives. *MRS Bull* 43(8):576–580. <https://doi.org/10.1557/mrs.2018.181>
- Gomah-Petry JR, Saïd S, Marchet P, Mercurio JP (2004) Sodium-bismuth titanate based lead-free ferroelectric materials. *J Eur Ceram Soc* 24(6):1165–1169. [https://doi.org/10.1016/S0955-2219\(03\)00473-4](https://doi.org/10.1016/S0955-2219(03)00473-4)
- Mishra A, Majumdar B, Ranjan R (2017) A complex lead-free (Na, Bi, Ba)(Ti, Fe)O<sub>3</sub> single phase perovskite ceramic with a high

- energy-density and high discharge-efficiency for solid state capacitor applications. *J Eur Ceram Soc* 37(6):2379–2384. <https://doi.org/10.1016/j.jeurceramsoc.2017.01.036>
16. Wang B, Luo L, Jiang X, Li W, Chen H (2014) Energy-storage properties of  $(1-x)\text{Bi}_{0.47}\text{Na}_{0.47}\text{Ba}_{0.06}\text{TiO}_3\text{-xKNbO}_3$  lead-free ceramics. *J Alloys Compd* 585:14–18. <https://doi.org/10.1016/j.jallcom.2013.09.052>
  17. Shi P, Zhu L, Gao W, Yu Z, Lou X, Wang X, Yang Z, Yang S (2019) Large energy storage properties of lead-free  $(1-x)(0.72\text{Bi}_{0.5}\text{Na}_{0.5}\text{TiO}_3\text{-}0.28\text{SrTiO}_3)\text{-xBiAlO}_3$  ceramics at broad temperature range. *J Alloys Compd* 784:788–793. <https://doi.org/10.1016/j.jallcom.2019.01.077>
  18. Gao J, Zhang Y, Zhao L, Lee KY, Liu Q, Studer A, Hinterstein M, Zhang S, Li JF (2019) Enhanced antiferroelectric phase stability in La-doped  $\text{AgNbO}_3$ : perspectives from the microstructure to energy storage properties. *J Mater Chem A* 7(5):2225–2232. <https://doi.org/10.1039/c8ta09353a>
  19. Tian Y, Jin L, Hu Q, Yu K, Zhuang Y, Viola G, Abrahams I, Xu Z, Wei X, Yan H (2019) Phase transitions in tantalum-modified silver niobate ceramics for high power energy storage. *J Mater Chem A* 7(2):834–842. <https://doi.org/10.1039/c8ta10075f>
  20. Zhang L, Hao X (2014) Dielectric properties and energy-storage performances of  $(1-X)(\text{Na}_{0.5}\text{Bi}_{0.5})\text{TiO}_3\text{-xSrTiO}_3$  thick films prepared by screen printing technique. *J Alloys Compd* 586:674–678. <https://doi.org/10.1016/j.jallcom.2013.10.107>
  21. Acosta M, Novak N, Rojas V, Patel S, Vaish R, Koruza J, Rossetti GA Jr, Rödel J (2017)  $\text{BaTiO}_3$ -based piezoelectrics: fundamentals, current status, and perspectives. *Appl Phys Rev* 4(4):041305. <https://doi.org/10.1063/1.4990046>
  22. Du XL, Wang XL, Li YH, Wang YL, Zhao JJ, Fang LJ, Zheng LR, Tong H, Yang HG (2017) Isolation of single Pt atoms in a silver cluster: forming highly efficient silver-based cocatalysts for photocatalytic hydrogen evolution. *Chem Commun* 53(68):9402–9405. <https://doi.org/10.1039/c7cc04061j>
  23. Benyoussef M, Zannen M, Belhadi J, Manoun B, Dellis JL, El Marsi M, Lahmar A (2018) Dielectric, ferroelectric, and energy storage properties in dysprosium doped sodium bismuth titanate ceramics. *Ceram Int* 44(16):19451–19460. <https://doi.org/10.1016/j.ceramint.2018.07.182>
  24. Zhang L, Hao X, Zhang L (2014) Enhanced energy-storage performances of  $\text{Bi}_2\text{O}_3\text{-Li}_2\text{O}$  added  $(1-x)(\text{Na}_{0.5}\text{Bi}_{0.5})\text{TiO}_3\text{-xBaTiO}_3$  thick films. *Ceram Int* 40(6):8847–8851. <https://doi.org/10.1016/j.ceramint.2014.01.107>
  25. Fan P, Zhang Y, Zhang ST, Xie B, Zhu Y, Marwat MA, Ma W, Liu K, Shu L, Zhang H (2019) Low-temperature sintered  $(\text{Na}_{1/2}\text{Bi}_{1/2})\text{TiO}_3$ -based incipient piezoceramics for co-fired multilayer actuator application. *J Mater* 5(3):480–488. <https://doi.org/10.1016/j.jmat.2019.01.004>
  26. Smolensky GA, Isupov VA, Agranovskaya AI, Krainik NN (1961) New materials of  $\text{A}_2\text{B}_4\text{O}_6$  type. *Trans Sov Phys Solid State* 2:2651–2654
  27. Paterson AR, Nagata H, Tan X, Daniels JE, Hinterstein M, Ranjan R, Groszewicz PB, Jo W, Jones JL (2018) Relaxor-ferroelectric transitions: sodium bismuth titanate derivatives. *MRS Bull* 43(8):600–606
  28. Spreitzer M, Valant M, Suvorov D (2007) Sodium deficiency in  $\text{Na}_{0.5}\text{Bi}_{0.5}\text{TiO}_3$ . *J Mater Chem* 17(2):185–192. <https://doi.org/10.1039/b609606a>
  29. Yilmaz H, Messing GL, Trolier-McKinstry S (2003) (Reactive) templated grain growth of textured sodium bismuth titanate  $(\text{Na}_{1/2}\text{Bi}_{1/2})\text{TiO}_3\text{-BaTiO}_3$  ceramics—I processing. *J Electroceram* 11(3):207–215. <https://doi.org/10.1023/B:JECR.0000026375.50590.81>
  30. Gao L, Huang Y, Hu Y, Du H (2007) Dielectric and ferroelectric properties of  $(1-x)\text{BaTiO}_3\text{-xBi}_{0.5}\text{Na}_{0.5}\text{TiO}_3$  ceramics. *Ceram Int* 33(6):1041–1046. <https://doi.org/10.1016/j.ceramint.2006.03.006>
  31. Das Adhikary G, Khatua DK, Senyshyn A, Ranjan R (2019) Random lattice strain and its relaxation towards the morphotropic phase boundary of  $\text{Na}_{0.5}\text{Bi}_{0.5}\text{TiO}_3$ -based piezoelectrics: impact on the structural and ferroelectric properties. *Phys Rev B* 99(17):174112. <https://doi.org/10.1103/PhysRevB.99.174112>
  32. Praharaj S, Rout D, Anwar S, Subramanian V (2017) Polar nano regions in lead free  $(\text{Na}_{0.5}\text{Bi}_{0.5})\text{TiO}_3\text{-SrTiO}_3\text{-BaTiO}_3$  relaxors: an impedance spectroscopic study. *J Alloys Compd* 706:502–510. <https://doi.org/10.1016/j.jallcom.2017.02.257>
  33. Kounga AB, Zhang ST, Jo W, Granzow T, Rödel J (2008) Morphotropic phase boundary in  $(1-x)\text{Bi}_{0.5}\text{Na}_{0.5}\text{TiO}_3\text{-xK}_{0.5}\text{Na}_{0.5}\text{NbO}_3$  lead-free piezoceramics. *Appl Phys Lett* 92(22):222902. <https://doi.org/10.1063/1.2938064>
  34. Khatua DK, Agarwal A, Mishra A, Das Adhikary G, Senyshyn A, Ranjan R (2018) Enhanced thermal stability of dielectric, energy storage, and discharge efficiency in a structurally frustrated piezoelectric system: Erbium modified  $\text{Na}_{0.5}\text{Bi}_{0.5}\text{TiO}_3\text{-BaTiO}_3$ . *J Appl Phys* 124(10):104101. <https://doi.org/10.1063/1.5035263>
  35. Takenaka T, Maruyama K, Sakata K (1991)  $(\text{Bi}_{1/2}\text{Na}_{1/2})\text{TiO}_3\text{-BaTiO}_3$  System for lead-free piezoelectric ceramics. *Jpn J Appl Phys* 30(9S):2236–2239. <https://doi.org/10.1111/j.1151-2916.1958.tb12903.x>
  36. Garg R, Narayana Rao B, Senyshyn A, Ranjan R (2013) Long ranged structural modulation in the pre-morphotropic phase boundary cubic-like state of the lead-free piezoelectric  $\text{Na}_{1/2}\text{Bi}_{1/2}\text{TiO}_3\text{-BaTiO}_3$ . *J Appl Phys* 114(23):234102. <https://doi.org/10.1063/1.4842855>
  37. Ranjan R, Dviwedi A (2005) Structure and dielectric properties of  $(\text{Na}_{0.50}\text{Bi}_{0.50})1\text{-xBa}_x\text{TiO}_3$ :  $0 \leq x \leq 0.10$ . *Solid State Commun* 135(6):394–399. <https://doi.org/10.1016/j.ssc.2005.03.053>
  38. Zhang ST, Kounga AB, Aulbach E (2008) Lead-free piezoceramics with giant strain in the system  $\text{Bi}_{0.5}\text{Na}_{0.5}\text{TiO}_3\text{-BaTiO}_3\text{-K}_{0.5}\text{Na}_{0.5}\text{NbO}_3$ . I. Structure and room temperature properties. *J Appl Phys* 103(3):034107. <https://doi.org/10.1063/1.2838472>
  39. Gao F, Dong X, Mao C, Cao F, Wang G (2012) Phase diagram of  $(1-x\%) (0.89\text{Bi}_{0.5}\text{Na}_{0.5}\text{TiO}_3\text{-}0.06\text{BaTiO}_3\text{-}0.05\text{K}_{0.5}\text{Na}_{0.5}\text{NbO}_3)\text{-}x\%\text{MnO}_2$  lead-free anti-ferroelectric ceramics. *Solid State Commun* 152(17):1670–1672. <https://doi.org/10.1016/j.ssc.2012.06.007>
  40. Jo W, Ollagnier JB, Park JL, Anton EM, Kwon OJ, Park C, Seo HH, Lee JS, Erdem E, Eichel RA, Rödel J (2011)  $\text{CuO}$  as a sintering additive for  $(\text{Bi}_{1/2}\text{Na}_{1/2})\text{TiO}_3\text{-BaTiO}_3\text{-(K}_{0.5}\text{Na}_{0.5})\text{NbO}_3$  lead-free piezoceramics. *J Eur Ceram Soc* 31(12):2107–2117. <https://doi.org/10.1016/j.jeurceramsoc.2011.05.008>
  41. Ma HY, Chen XM, Wang J, Huo KT, Lian HL, Liu P (2013) Structure, dielectric and ferroelectric properties of  $0.92\text{Na}_{0.5}\text{Bi}_{0.5}\text{TiO}_3\text{-}0.06\text{BaTiO}_3\text{-}0.02\text{K}_{0.5}\text{Na}_{0.5}\text{NbO}_3$  lead-free ceramics: effect of  $\text{Co}_2\text{O}_3$  additive. *Ceram Int* 39(4):3721–3729. <https://doi.org/10.1016/j.ceramint.2012.10.208>
  42. Chauhan A, Patel S, Vaish R (2014) Mechanical confinement for improved energy storage density in BNT-BT-KNN lead-free ceramic capacitors. *AIP Adv* 4(8):087106. <https://doi.org/10.1063/1.4892608>
  43. Chandrasekhar M, Kumar P (2016) Synthesis and characterizations of BNT-BT-KNN ceramics for energy storage applications. *Phase Transit* 89(9):944–957. <https://doi.org/10.1080/01411594.2015.1118763>
  44. Gao F, Dong X, Mao C, Liu W, Zhang H, Yang L, Cao F, Wang G (2011) Energy-storage properties of  $0.89\text{Bi}_{0.5}\text{Na}_{0.5}\text{TiO}_3\text{-}0.06\text{BaTiO}_3\text{-}0.05\text{K}_{0.5}\text{Na}_{0.5}\text{NbO}_3$  lead-free anti-ferroelectric ceramics. *J Am Ceram Soc* 94(12):4382–4386. <https://doi.org/10.1111/j.1551-2916.2011.04731.x>



45. Ding J, Liu Y, Lu Y, Qian H, Gao H, Chen H, Ma C (2014) Enhanced energy-storage properties of  $0.89\text{Bi}_{0.5}\text{Na}_{0.5}\text{TiO}_3-0.06\text{BaTiO}_3-0.05\text{K}_{0.5}\text{Na}_{0.5}\text{NbO}_3$  lead-free anti-ferroelectric ceramics by two-step sintering method. *Mater Lett* 114:107–110. <https://doi.org/10.1016/j.matlet.2013.09.103>
46. Dittmer R, Jo W, Damjanovic D, Rödel J (2014) Lead-free high-temperature dielectrics with wide operational range. *J Appl Phys* 109(3):034107
47. Gao F, Dong X, Mao C, Cao F, Wang G (2011) c/a Ratio-dependent energy-storage density in  $(0.9-x)\text{Bi}_{0.5}\text{Na}_{0.5}\text{TiO}_3-x\text{BaTiO}_3-0.1\text{K}_{0.5}\text{Na}_{0.5}\text{NbO}_3$  ceramics. *J Am Ceram Soc* 94(12):4162–4164
48. Ogihara H, Randall CA, Trolier-McKinstry S (2009) Weakly coupled relaxor behavior of  $\text{BaTiO}_3\text{-BiScO}_3$  ceramics. *J Am Ceram Soc* 92(1):110–118. <https://doi.org/10.1111/j.1551-2916.2008.02798.x>
49. Schneider CA, Rasband WS, Eliceiri KW (2012) NIH Image to ImageJ: 25 years of image analysis. *Nat Methods* 9(7):671
50. Carvajal JR (2000) FULLPROF. A rietveld refinement and pattern matching analysis program. Laboratoire Leon Brillouin, CEA-CNRS, France
51. Zou K, Dan Y, Xu H, Zhang Q, Lu Y, Huang H, He Y (2019) Recent advances in lead-free dielectric materials for energy storage. *Mater Res Bull* 113:190–201. <https://doi.org/10.1016/j.materresbull.2019.02.002>
52. Wang G, Lu Z, Zhang Z, Feteira A, Tang CC, Hall DA (2019) Electric field-induced irreversible relaxor to ferroelectric phase transformations in  $\text{Na}_{0.5}\text{Bi}_{0.5}\text{TiO}_3\text{-NaNbO}_3$  ceramics. *J Am Ceram Soc* 102(12):7746–7754. <https://doi.org/10.1111/jace.16676>
53. Khatua DK, Mishra A, Kumar N, Adhikary GD, Shankar U, Majumdar B, Ranjan R (2019) A coupled microstructural-structural mechanism governing thermal depolarization delay in  $\text{Na}_{0.5}\text{Bi}_{0.5}\text{TiO}_3$ -based piezoelectrics. *Acta Mater* 179:49–60. <https://doi.org/10.1016/j.actamat.2019.08.022>
54. Mishra A, Khatua DK, Das AG, Kumar N, Shankar U, Ranjan R (2019) Finite-size-effect on a very large length scale in NBT-based lead-free piezoelectrics. *J Adv Dielectr* 9(5):1950035. <https://doi.org/10.1142/S2010135X19500358>
55. Seo IT, Steiner S, Frömling T (2017) The effect of A site nonstoichiometry on  $0.94(\text{Na}_y\text{Bi}_x)\text{TiO}_3-0.06\text{BaTiO}_3$ . *J Eur Ceram Soc* 37(4):1429–1436. <https://doi.org/10.1016/j.jeurceramsoc.2016.11.045>
56. Hennings DFK, Janssen R, Reynen PJL (1987) Control of liquid-phase-enhanced discontinuous grain growth in barium titanate. *J Am Ceram Soc* 70(1):23–27. <https://doi.org/10.1111/j.1151-2916.1987.tb04847.x>
57. German RM, Rabin BH (1985) Enhanced sintering through second phase additions. *Powder Metall* 28(1):7–12. <https://doi.org/10.1179/pom.1985.28.1.7>
58. Senda T, Bradt RC (1990) Grain growth in sintered ZnO and ZnO-Bi<sub>2</sub>O<sub>3</sub> ceramics. *J Am Ceram Soc* 73(1):106–114. <https://doi.org/10.1111/j.1151-2916.1990.tb05099.x>
59. Garg R, Rao BN, Senyshyn A, Krishna PSR, Ranjan R (2013) Lead-free piezoelectric system  $(\text{Na}_{0.5}\text{Bi}_{0.5})\text{TiO}_3\text{-BaTiO}_3$ : equilibrium structures and irreversible structural transformations driven by electric field and mechanical impact. *Phys Rev B: Condens Matter Mater Phys* 88(1):014103. <https://doi.org/10.1103/PhysRevB.88.014103>
60. Jo W, Daniels JE, Jones JL, Tan X, Thomas PA, Damjanovic D, Rödel J (2011) Evolving morphotropic phase boundary in lead-free  $(\text{Bi}_{1/2}\text{Na}_{1/2})\text{TiO}_3\text{-BaTiO}_3$  piezoceramics. *J Appl Phys* 109(1):014110. <https://doi.org/10.1063/1.3530737>
61. Tellier J, Malic B, Dkhil B, Jenko D, Cilensek J, Kosec M (2009) Crystal structure and phase transitions of sodium potassium niobate perovskites. *Sol Stat Sci* 11(2):320–324. <https://doi.org/10.1016/j.solidstatesciences.2008.07.011>
62. Chu SY, Water W, Juang YD, Liaw JT (2003) Properties of  $(\text{Na,K})\text{NbO}_3$  and  $(\text{Li,Na,K})\text{NbO}_3$  ceramic mixed systems. *Ferroelectrics* 287(1):23–33. <https://doi.org/10.1080/00150190390200767>
63. Rao BN, Datta R, Chandrashekar SS, Mishra DK, Sathe V, Senyshyn A, Ranjan R (2013) Local structural disorder and its influence on the average global structure and polar properties in  $\text{Na}_{0.5}\text{Bi}_{0.5}\text{TiO}_3$ . *Phys Rev B* 88(22):224103. <https://doi.org/10.1103/PhysRevB.88.224103>
64. Rao BN, Fitch AN, Ranjan R (2013) Ferroelectric-ferroelectric phase coexistence in  $\text{Na}_{1/2}\text{Bi}_{1/2}\text{TiO}_3$ . *Phys Rev B* 87(6):060102. <https://doi.org/10.1103/PhysRevB.87.060102>
65. Rao BN, Ranjan R (2012) Electric-field-driven monoclinic-to-rhombohedral transformation in  $\text{Na}_{1/2}\text{Bi}_{1/2}\text{TiO}_3$ . *Phys Rev B* 86(13):134103. <https://doi.org/10.1103/PhysRevB.86.134103>
66. Khatua DK, Senyshyn A, Ranjan R (2016) Long-period modulated structure and electric-field-induced structural transformation in  $\text{Na}_{0.5}\text{Bi}_{0.5}\text{TiO}_3$ -based lead-free piezoelectrics. *Phys Rev B* 93(13):134106. <https://doi.org/10.1103/PhysRevB.93.134106>
67. Park SE, Chung SJ, Kim IT, Hong KS (1994) Nonstoichiometry and the long-range cation ordering in crystals of  $(\text{Na}_{1/2}\text{Bi}_{1/2})\text{TiO}_3$ . *J Am Ceram Soc* 77(10):2641–2647. <https://doi.org/10.1111/j.1151-2916.1994.tb04655.x>
68. Ishchuk VM, Gusakova LG, Kisel NG, Spiridonov NA, Sobolev VL (2016) Zr-Substituted  $(\text{Na}_{0.5}\text{Bi}_{0.5})_{1-x}\text{Ba}_x\text{TiO}_3$ -based solid solutions. *J Am Ceram Soc* 99(5):1786–1791. <https://doi.org/10.1111/jace.14140>
69. Xu D, Shi L, Wu Z, Zhong Q, Wu X (2009) Microstructure and electrical properties of ZnO-Bi<sub>2</sub>O<sub>3</sub>-based varistor ceramics by different sintering processes. *J Eur Ceram Soc* 29(9):1789–1794. <https://doi.org/10.1016/j.jeurceramsoc.2008.10.020>
70. Kracek FC (2002) The system sodium oxide-silica. *J Phys Chem* 34(7):1583–1598. <https://doi.org/10.1021/j150313a018>
71. Ul-Hamid A, Tawancy HM, Mohammed ARI, Al-Jaroudi SS, Abbas NM (2006) Quantitative WDS analysis using electron probe microanalyzer. *Mater Character* 56(3):192–199. <https://doi.org/10.1016/j.matchar.2005.11.007>
72. Fournier C, Merlet C, Dugne O, Fialin M (1999) Standardless semi-quantitative analysis with WDS-EPMA. *J Anal Atom Spect* 14(3):381–386. <https://pubs.rsc.org/en/content/articlehtml/1999/ja/a807433j>
73. Shi X, Kumar N, Hoffman M (2020) Electrical fatigue behavior of NBT-BT-xKNN ferroelectrics: effect of ferroelectric phase transformations and oxygen vacancies. *J Mater Chem C* 8(11):3887–3896. <https://pubs.rsc.org/lu/content/articlehtml/2020/tc/c9tc05665c>
74. Lalitha KV, Riemer LM, Koruza J, Rödel J (2017) Hardening of electromechanical properties in piezoceramics using a composite approach. *Appl Phys Lett* 111(2):022905. <https://doi.org/10.1063/1.4986911>
75. Luo H, Ke H, Zhang H, Zhang L, Li F, Cao L, Jia D, Zhou Y (2019) Enhanced ferroelectric and energy-storage properties of Nb-doped  $0.94\text{Na}_{0.5}\text{Bi}_{0.5}\text{TiO}_3-0.06\text{BaTiO}_3$  ceramics prepared by a multi-ionic sol-gel method. *Phys B: Cond Matt* 567:17–24. <https://doi.org/10.1016/j.physb.2019.05.008>
76. Riemer LM, Lalitha KV, Jiang X, Liu N, Dietz C, Stark RW, Groszewicz PB, Buntkowsky G, Chen J, Zhang ST, Roedel J (2017) Stress-induced phase transition in lead-free relaxor ferroelectric composites. *Acta Mater* 136:271–280. <https://doi.org/10.1016/j.actamat.2017.07.008>
77. Steiner S, Seo IT, Ren P, Li M, Keeble DJ, Frömling T (2019) The effect of Fe-acceptor doping on the electrical properties of  $\text{Na}_{1/2}\text{Bi}_{1/2}\text{TiO}_3$  and  $0.94(\text{Na}_{1/2}\text{Bi}_{1/2})\text{TiO}_3-0.06\text{BaTiO}_3$ . *J Am Ceram Soc* 102(9):5295–5304. <https://doi.org/10.1111/jace.16401>
78. Zhang J, Pan Z, Guo FF, Liu WC, Ning H, Chen YB, Lu MH, Yang B, Chen J, Zhang ST, Xing X, Rodel J, Cao W, Chen YF (2015) Semiconductor/relaxor 0–3 type composites without thermal

- depolarization in  $\text{Bi}_{0.5}\text{Na}_{0.5}\text{TiO}_3$ -based lead-free piezoceramics. *Nat Commun* 6(1):1–10. <https://doi.org/10.1038/ncomms7615>
79. Mishra A, Khatua DK, De A, Majumdar B, Frömling T, Ranjan R (2019) Structural mechanism behind piezoelectric enhancement in off-stoichiometric  $\text{Na}_{0.5}\text{Bi}_{0.5}\text{TiO}_3$  based lead-free piezoceramics. *Acta Mater* 164:761–775. <https://doi.org/10.1016/j.actamat.2018.11.015>
80. Mishra A, Khatua DK, De A, Ranjan R (2019) Off-stoichiometry, structural-polar disorder and piezoelectricity enhancement in pre-MPB lead-free  $\text{Na}_{0.5}\text{Bi}_{0.5}\text{TiO}_3$ - $\text{BaTiO}_3$  piezoceramic. *J Appl Phys* 125(21):214101. <https://doi.org/10.1063/1.5089123>
81. Maurya D, Pramanick A, Feyngenson M, Neufeind JC, Bodnar RJ, Priya S (2014) Effect of poling on nanodomains and nanoscale structure in A-site disordered lead-free piezoelectric  $\text{Na}_{0.5}\text{Bi}_{0.5}\text{TiO}_3$ - $\text{BaTiO}_3$ . *J Mater Chem C* 2(39):8423–8431. <https://doi.org/10.1039/c4tc01124d>
82. Kumar N, Mishra A, De A, Shankar U, Ranjan R (2020) Factors contributing to the local polar-structural heterogeneity and ultrahigh piezoelectricity in Sm-modified  $\text{Pb}(\text{Mg}_{1/3}\text{Nb}_{2/3})\text{O}_3$ - $\text{PbTiO}_3$ . *J Phys D Appl Phys* 53(16):165302. <https://doi.org/10.1088/1361-6463/ab6ea2>
83. Khatua DK, Kalaskar A, Ranjan R (2016) Tuning photoluminescence response by electric field in electrically soft ferroelectrics. *Phys Rev Lett* 116(11):117601. <https://doi.org/10.1103/PhysRevLett.116.117601>
84. Chandrasekhar M, Jayarao G, Khatua DK, Kumar P (2019) Effect of  $\text{NaNbO}_3$  addition on structure, dielectric and energy storage properties of lead free piezoelectric  $\text{Bi}_{0.5}\text{Na}_{0.5}\text{TiO}_3$ - $\text{K}_{0.5}\text{Na}_{0.5}\text{NbO}_3$  ceramics. *Ceram Int* 45(2):1969–1976. <https://doi.org/10.1016/j.ceramint.2018.10.091>
85. Ren P, He J, Yan F, Wang X (2019) Temperature-stable dielectric and energy storage properties of  $(1-x)(0.94\text{Bi}_{0.5}\text{Na}_{0.5}\text{TiO}_3-0.09\text{BiAlO}_3)$ - $x\text{SrTiO}_3$  ceramics. *J Alloy Comp* 807:151676. <https://doi.org/10.1016/j.jallcom.2019.151676>
86. Hu Q, Tian Y, Zhu Q, Bian J, Jin L, Du H, Alikin DO, Shur VY, Feng Y, Xu Z, Wei X (2020) Achieve ultrahigh energy storage performance in  $\text{BaTiO}_3$ - $\text{Bi}(\text{Mg}_{1/2}\text{Ti}_{1/2})\text{O}_3$  relaxor ferroelectric ceramics via nano-scale polarization mismatch and reconstruction. *Nano Energy* 67:104264. <https://doi.org/10.1016/j.nanoen.2019.104264>
87. Qi H, Xie A, Tian A, Zuo R (2020) Superior energy-storage capacitors with simultaneously giant energy density and efficiency using nanodomain engineered  $\text{BiFeO}_3$ - $\text{BaTiO}_3$ - $\text{NaNbO}_3$  lead-free bulk ferroelectrics. *Adv Ener Mater* 10(6):1903338. <https://doi.org/10.1002/aenm.2019033>
88. Yang H, Liu P, Yan F, Lin Y, Wang T (2019) A novel lead-free ceramic with layered structure for high energy storage applications. *J Alloy Comp* 773:244–249. <https://doi.org/10.1016/j.jallcom.2018.09.252>
89. Zhang L, Pu Y, Chen M (2019) Influence of  $\text{BaZrO}_3$  additive on the energy-storage properties of  $0.775\text{Na}_{0.5}\text{Bi}_{0.5}\text{TiO}_3-0.225\text{BaSnO}_3$  relaxor ferroelectrics. *J Alloy Comp* 775:342–347. <https://doi.org/10.1016/j.jallcom.2018.10.025>
90. Li Q, Li M, Wang C, Zhang M, Fan H (2019) Enhanced temperature stable dielectric properties and energy-storage density of  $\text{BaSnO}_3$ -modified  $(\text{Bi}_{0.5}\text{Na}_{0.5})_{0.94}\text{Ba}_{0.06}\text{TiO}_3$  lead-free ceramics. *Ceram Int* 45(16):19822–19828. <https://doi.org/10.1016/j.ceramint.2019.06.237>
91. Wang H, Hu Q, Liu X, Zheng Q, Jiang N, Yang Y, Kwok KW, Xu C, Lin D (2019) A high-tolerance BNT-based ceramic with excellent energy storage properties and fatigue/frequency/thermal stability. *Ceram Int* 45(17):23233–23240. <https://doi.org/10.1016/j.ceramint.2019.08.019>
92. Ma W, Fan P, Salamon D, Kongparakul S, Samart C, Zhang T, Zhang G, Jiang S, Chang JJ, Zhang H (2019) Fine-grained BNT-based lead-free composite ceramics with high energy-storage density. *Ceram Int* 45(16):19895–19901. <https://doi.org/10.1016/j.ceramint.2019.06.245>
93. Sui J, Fan H, Peng H, Ma J, Yadav AK, Chao W, Zhang M, Dong G (2019) Enhanced energy-storage performance and temperature-stable dielectric properties of  $(1-x)[(\text{Na}_{0.5}\text{Bi}_{0.5})_{0.95}\text{Ba}_{0.05}]_{0.98}\text{La}_{0.02}\text{TiO}_3-x\text{K}_{0.5}\text{Na}_{0.5}\text{NbO}_3$  lead-free ceramics. *Ceram Int* 45(16):20427–20434. <https://doi.org/10.1016/j.ceramint.2019.07.019>
94. Liu G, Li Y, Shi M, Yu L, Chen P, Yu K, Yan Y, Jin L, Wang D, Gao J (2019) An investigation of the dielectric energy storage performance of  $\text{Bi}(\text{Mg}_{2/3}\text{Nb}_{1/3})\text{O}_3$ -modified  $\text{BaTiO}_3$  Pb-free bulk ceramics with improved temperature/frequency stability. *Ceram Int* 45(15):19189–19196. <https://doi.org/10.1016/j.ceramint.2019.06.166>
95. Liu X, Yang H, Yan F, Qin Y, Lin Y, Wang T (2019) Enhanced energy storage properties of  $\text{BaTiO}_3$ - $\text{Bi}_{0.5}\text{Na}_{0.5}\text{TiO}_3$  lead-free ceramics modified by  $\text{SrY}_{0.5}\text{Nb}_{0.5}\text{O}_3$ . *J Alloy Comp* 778:97–104. <https://doi.org/10.1016/j.jallcom.2018.11.106>
96. Zhou M, Liang R, Zhou Z, Dong X (2019) Combining high energy efficiency and fast charge-discharge capability in novel  $\text{BaTiO}_3$ -based relaxor ferroelectric ceramic for energy-storage. *Ceram Int* 45(3):3582–3590. <https://doi.org/10.1016/j.ceramint.2018.11.018>
97. Lin Y, Li D, Zhang M, Zhan S, Yang Y, Yang H, Yuan Q (2019) Excellent energy-storage properties achieved in  $\text{BaTiO}_3$ -based lead-free relaxor ferroelectric ceramics via domain engineering on the nanoscale. *ACS Appl Mater Int* 11(40):36824–36830. <https://doi.org/10.1021/acsami.9b10819>
98. Ma W, Zhu Y, Marwat MA, Fan P, Xie B, Salamon D, Ye ZG, Zhang H (2019) Enhanced energy-storage performance with excellent stability under low electric fields in BNT-ST relaxor ferroelectric ceramics. *J Mater Chem C* 7(2):281–288. <https://doi.org/10.1039/C8TC04447C>
99. Zhao P, Wang H, Wu L, Chen L, Cai Z, Li L, Wang X (2019) High-performance relaxor ferroelectric materials for energy storage applications. *Adv Energy Mater* 9(17):1803048. <https://doi.org/10.1002/aenm.201803048>

**Publisher's Note** Springer Nature remains neutral with regard to jurisdictional claims in published maps and institutional affiliations